Draft 1

Precision Measurements of the Electromagnetic Properties of Pseudoscalar Mesons at 11 GeV via the Primakoff Effect

TJNAF White Paper

The PrimEx Collaboration

May 26, 2000

Contents

1 Introduction **3**

2 Motivation **3**

3 Radiative Widths of Pseudoscalar Mesons **7**
- 3.1 Radiative width of the π^o . . . 7
- 3.2 Radiative Widths of the η and η' with 11 GeV . . . 9
  - 3.2.1 Motivation . . . 9
  - 3.2.2 Previous Measurments of the η and η' Radiative Widths . . . 9
  - 3.2.3 Measurement of the η and η' Radiative Widths via the Primakoff Effect 10
  - 3.2.4 Experimental Setup for η/η' Width Measurement . . . 16
  - 3.2.5 Zero Degree Virtual Photon Tagging System . . . 16
  - 3.2.6 Low-Energy Recoil Detection . . . 21
  - 3.2.7 Importance of Low-Energy Recoil Detection . . . 21
  - 3.2.8 Scientific Evaluation of the Low Pressure Chamber Technique . . . 23
  - 3.2.9 Low Energy Recoil detector based on LPMWPCs . . . 26
  - 3.2.10 The Hybrid Calorimeter (HYCAL) . . . 33
  - 3.2.11 Lead Glass Detectors . . . 33
  - 3.2.12 Lead Tungstate Detectors . . . 34
  - 3.2.13 Background Veto Detector . . . 35
  - 3.2.14 Rates and Uncertainties . . . 42

4 Measurements of the Transition Form Factors $F_{\gamma\gamma^* P}$ **42**
- 4.1 Previous Measurements in the Space-like Region . . . 48
- 4.2 Previous Experiments in the Time-like Region . . . 49
- 4.3 The Proposed Experiment . . . 50
  - 4.3.1 Experimental Setup for Transition Form Factor Measurements . . . 51
  - 4.3.2 Rates for $F_{\gamma\gamma^*\pi^o}$ and $F_{\gamma\gamma^*\eta^o}$ . . . 52

5 Summary **54**

1 Introduction

The future availability of high quality, high duty factor 11 GeV electron beams at TJNAF will enable new, unprecedented opportunities to perform precise measurements of meson decay widths and electromagnetic transition form factors. Here, we detail how one can exploit the high energy electro- and photoproduction of pseudoscalar mesons in the Coulomb field of a nucleus, the so called Primakoff effect, to study the two photon decay widths, $\Gamma_{\gamma\gamma}$, and the transition form factors, $F_{\gamma\gamma^* P}$, where P represents the π^o, η, and η' pseudoscalar mesons. This comprehensive program will provide fundamental tests of both quantum chromodynamics and QCD inspired models.

In addition to the proposed 11 GeV upgrade to the CEBAF accelerator, this program will require the construction of some ancillary instrumentation including (1), a magnetic spectrometer for a virtual photon tagging facility, (2) a hybrid calorimeter for detection of multiphoton states and in some cases, scattered electrons, and (3) a recoil detector based on low pressure multiwire proportional chambers. The requirements for this instrumention are described below.

2 Motivation

The three neutral pseudoscalar mesons π^0, η and η' represent one of the most interesting systems in strong interactions. This system contains fundamental information about the effects of SU(3) and isospin breaking by the u, d, and s quark masses, leading to important mixing effects among the mesons, as well as about two types of chiral anomalies, namely, the $U_A(1)$ anomaly that involves the flavor singlet axial current $j^\mu_A = \bar{q}\gamma^\mu\gamma_5 q$ and the color currents, and the anomalies involving either the singlet axial current or one of the two neutral axial currents $j^\mu_{A3} = \bar{q}\gamma^\mu\gamma_5\lambda_3 q$ and $j^\mu_{A8} = \bar{q}\gamma^\mu\gamma_5\lambda_8 q$, where $q = (u, d, s)^T$ and two electromagnetic currents. The first anomaly involves the triangle diagram of figure(1). This diagram gives a non-vanishing divergence to the $U_A(1)$ current:

$$\partial_\mu j^\mu_A = \frac{3\alpha_s}{8\pi}\epsilon^{\mu\nu\rho\sigma} G^a_{\mu\nu} G^a_{\rho\sigma},$$

where G are the gluon fields.

The second type of anomaly results from diagrams as in figure(2). These lead to similar non-conservation equations as the above one. Explicitly:

$$\partial_\mu j^\mu_{A3} = \frac{N_c\alpha_{em}}{3\pi}\epsilon^{\mu\nu\rho\sigma} F_{\mu\nu} F\rho\sigma$$

$$\partial_\mu j^\mu_{A8} = \frac{1}{\sqrt{3}}\frac{\alpha_{em}}{3\pi}\epsilon^{\mu\nu\rho\sigma} F_{\mu\nu} F_{\rho\sigma}$$

as well as an extra term on the right hand side of eqn.(1): $\sqrt{\frac{8}{3}}\frac{N_c\alpha_s}{3\pi}\epsilon^{\mu\nu\rho\sigma} F_{\mu\nu} F_{\rho\sigma}$, where F are the electromagnetic fields. These anomalies play a crucial role in the physics of the (π^0, η, η')

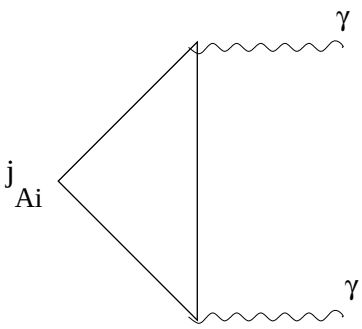

Figure 1:

complex; the $U_A(1)$ anomaly being responsible for large contributions to the η' mass and the others for the decays of the three mesons into photon pairs.

Since the quark masses are small, it is possible to quantify the effects due to their masses using perturbation theory (Chiral Perturbation Theory (ChPT)). In the chiral limit (limit of vanishing quark masses) the π^0 and η are Goldstone Bosons, belonging to an octet of SU(3), and their masses would vanish exactly, while the η' would be a singlet of SU(3) and acquire a mass due to the axial anomaly accompanied by the instanton configurations of the gluon fields. The η' mass in this limit is given in terms of the so called topological susceptibility. This susceptibility is of non-perturbative origin, and therefore difficult to calculate from first principles. So far some attempts have been made using lattice QCD, but the results remain uncertain. Given this situation, the mass of the η' is taken as input. In the chiral limit the second type of anomalies lead to a rigorous prediction of the decay amplitudes into two photons:

$$A(\pi^0 \to \gamma\gamma) = A_{\pi^0\gamma\gamma}\epsilon^{\mu\nu\rho\sigma}\epsilon_\mu\epsilon'_\nu k_\rho k'_\sigma$$
$$A(\eta \to \gamma\gamma) = A_{\eta_8\gamma\gamma}\epsilon^{\mu\nu\rho\sigma}\epsilon_\mu\epsilon'_\nu k_\rho k'_\sigma$$
$$A(\eta' \to \gamma\gamma) = A_{\eta_1\gamma\gamma}\epsilon^{\mu\nu\rho\sigma}\epsilon_\mu\epsilon'_\nu k_\rho k'\sigma,$$

where ϵ and k represent photon polarizations and momenta, and $A_{\pi^0\gamma\gamma} = \frac{\alpha_{em}}{8\pi F_\pi}$, $A_{\eta_8\gamma\gamma} = \frac{\alpha_{em}}{8\sqrt{3}\pi F_\eta}$, $A_{\eta_1\gamma\gamma} = \frac{\alpha_{em}}{\sqrt{24}\pi F'_\eta}$ where the $F's$ are the corresponding meson decay constants. While in

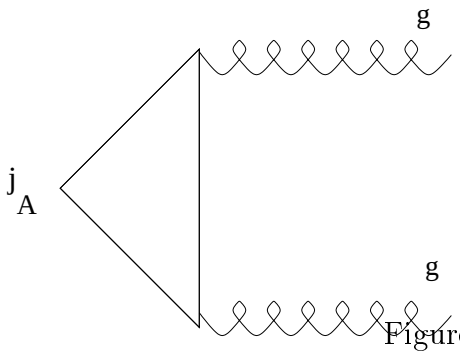

Figure 2:

the chiral limit SU(3) symmetry implies that $F_\pi = F_\eta$, $F_{\eta'}$ is not constrained by symmetries. However, in the limit of large number of colors in QCD (large N_c limit), one has $F_{\eta'} = F_\pi$.

The relatively straightforward situation of the chiral limit becomes much more complex in the real world with non-vanishing quark masses. In the real world the current quark masses are estimated to be $m_u \sim m_d/2 \sim 5$ MeV and $m_s \sim 150$ MeV. These masses make the π^0 and the η massive and shift the mass of the η' due to explicit breaking of chiral symmetry, and the breaking of SU(3) and isospin breaking induce mixing among the three mesons. The mixing is expressed in terms of three mixing angles; writing on the left the eigenstates of the chiral limit:

$$\pi_8^0 = \pi^0 - \epsilon\eta - \epsilon'\eta'$$

$$\eta_8 = cos\theta(\eta + \epsilon\pi^0) + sin\theta(\eta' + \epsilon'\pi^0)$$

$$\eta_1 = -sin\theta(\eta + \epsilon\pi^0) + cos\theta(\eta' + \epsilon'\pi^0)$$

The mixing angle ϵ is predicted in ChPT to be approximately -0.55^o. For the other two angles there are no rigorous predictions. If the large N_c limit holds without large corrections, then there is a prediction: $\epsilon' \sim -0.25^o$ and $\theta \sim -22^o$. It is so far unknown how large the deviations from the large N_c limit are, but expectations are that they are reasonably small. The angles ϵ and ϵ' play a role in the lifetime of the π^0, decreasing the lifetime by approximately 2%. For this proposal the relevant mixing angle is θ, and its value could be

determined experimentally by the effect the mixing has on the decay rates of the η and η' into two photons. The amplitudes are then given by:

$$A(\eta \to \gamma\gamma) = \frac{\alpha_{em}}{8\pi}(\frac{cos\theta}{\sqrt{3}F_\eta} - \sqrt{\frac{8}{3}}\frac{sin\theta}{F_{\eta'}})\epsilon^{\mu\nu\rho\sigma}\epsilon_\mu\epsilon'_\nu k_\rho k'_\sigma$$

$$A(\eta' \to \gamma\gamma) = \frac{\alpha_{em}}{8\pi}(\frac{sin\theta}{\sqrt{3}F_\eta} + \sqrt{\frac{8}{3}}\frac{cos\theta}{F_{\eta'}})\epsilon^{\mu\nu\rho\sigma}\epsilon_\mu\epsilon'_\nu k_\rho k'_\sigma,$$

where F_η is predicted in ChPT to be 1.3 F_π. For F'_η there is no independent determination, and theory can only give a rough estimate based on large N_c, where $F'_\eta \sim F_\pi$. The two amplitudes above would determine the mixing angle and F'_η if one measures the decay rates into two photons (or production rates as proposed here). There is, however, still one source of theoretical uncertainty which has to do with the possibility of corrections proportional to m_s that affect the relation between the anomaly and the decay amplitudes. These corrections are expected to be small in the case of the π^0 where they are instead proportional to $m_u + m_d$ (rough estimates in this case give corrections of the order of 1% in the rate). In the case of the η and η', with the assumption of validity of large N_c limit, an estimate [**?**] suggests that the corrections will be of the order of 6% in the amplitude. This latter correction can be hidden by correcting the values of F_η and F'_η entering in the two photon amplitudes. Unless the F'_η as determined by the coupling of the η' to the $U_A(1)$ current could be determined experimentally, a task that seems impossible, these effects cannot be pinned down experimentally. On the other hand, the mixing effect increases the amplitude by a factor of two; thus, the effect discussed before is much smaller. Indeed, these effects are proportional to m_s. While the effect of mixing on $\Gamma(\eta \to \gamma\gamma)$ is enhanced by the large coefficient that the amplitude for the η' has, all other effects are expected to be smaller and of similar magnitude.

More precise measurements of $\Gamma(\eta \to \gamma\gamma)$ and $\Gamma(\eta' \to \gamma\gamma)$ are crucial to the understanding of the mixing of the two mesons. The measurements of the first width have been carried out using the Primakoff effect [**?**] and $\gamma - \gamma$ fusion in $e^+ - e^-$ colliders [**?**], both determinations being in clear disagreement, while the second width has been only measured in $e^+ - e^-$ colliders [**?**]. The current results for the widths are:

$$\Gamma(\eta \to \gamma\gamma)_{\text{Primakoff}} = 324 \pm 46 \text{ eV}$$

$$\Gamma(\eta \to \gamma\gamma)_{\text{Collider}} = 510 \pm 26 \text{ eV}$$

$$\Gamma(\eta' \to \gamma\gamma)_{\text{Collider}} = 4.27 \pm 0.19 \text{ keV}$$

Fitting with the amplitudes of equation (4), one obtains respectively: $\theta = -16^0$, $F_{\eta'} = 100$ MeV, and $\theta = -22^0$, $F_{\eta'} = 95$ MeV. Independent of the uncertainties mentioned above, a new Primakoff measurement of the η decay and a first of the η' can lead to a clarification and a reasonably precise determination of the mixing angle θ.

The measurement of the radiative width of the η will also have an impact on other observables such as the $\eta \to \pi\pi\pi$ partial width, which is determined through the radiative

width and the $\eta \to \pi\pi\pi$ branching ratio. The current uncertainty in the $\eta \to \pi\pi\pi$ partial width is mostly due to the uncertainty in the radiative width.

Using Primakoff electroproduction it is also possible to gain access to the form factors for one virtual photon in the two photon mode. So far, the form factors have been determined in collider experiments [**?**], where $Q^2 \geq 0.6$ GeV^2, except for the form factor for the η' measured by the L3 collaboration where Q^2 is as low as 0.05 GeV^2. Measurements of the π^0, η and η' form factors down to low Q^2 are possible and very desirable. Such a measurement carried out with sufficient statistics can constrain and even determine the slope of the form factor. Currently there is no first principles theoretical determination of the form factors. In ChPT there are two sources of contributions [**?**], one is the long distance contribution from meson loops, and the other is a counterterm or short distance contribution. ChPT pins down the first, and for the second a model is needed. The long distance contributions are small, as they only provide a small fraction of the fall off of the form factor. The simplest model is to neglect the long distance contributions and assume a monopole type form factor,

$$F(Q^2) = \frac{\Lambda^2}{Q^2 + \Lambda^2}.$$

using such a model, the available data fits very well with a scale $\Lambda \sim 0.75 - 0.85$ GeV. If long distance contributions are included, a small change in these values results. The vector meson dominace (VMD) model is therefore an excellent model to fit the current data.

A determination of the slope of the π^0 and η form factors would allow one to fix one low energy constant in the effective chiral Lagrangian of order sixth [**?**]. If the η' form factor slope can also be measured, then one could have a reasonable test of how good the U(3) flavor symmetry implied by the large N_c limit holds. In this limit the same low energy term of order sixth should determine all slopes.

3 Radiative Widths of Pseudoscalar Mesons

3.1 Radiative width of the π^o

The two-photon partial decay widths of the π^o, η, and η' are of fundamental importance in QCD. The two-photon decay mode of the 0^- mesons reveals one of the most profound symmetry issues in QCD, namely, the explicit breaking of a classical symmetry by the quantum fluctuations of the quark fields coupling to a gauge field[**?**]. This phenomenon, called anomalous symmetry breaking, is of pure quantum mechanical origin. In QCD, there are several observable phenomena that originate from anomalies. One is connected with the couplings of the quarks to the gluons. This is the so called axial anomaly by which the conservation of the axial U(1) symmetry of the classical Lagrangian of QCD is broken in the limit where two or more quarks are massless, and the divergence of the corresponding axial-vector current becomes proportional to the product $\vec{E}^a \cdot \vec{B}^a$ of the chromo-electric and chromo-magnetic fields. The axial anomaly of interest to us involves the corresponding coupling of the quarks to photons[**?**]. In the case of the π^o, the coupling is to the isotriplet axial-vector current $\bar{q}\ I_3\ \gamma_\mu\gamma_5\ q$, where $q = (u,\ d)$, and I_3 is the third isospin generator.

If we limit ourselves to two quark flavors, the electromagnetic current is given by $\bar{q}\ (1/6 + I_3/2)\ \gamma_\mu\ q$. When coupling to the photon, the isosinglet and isotriplet components of the electromagnetic current lead to an anomaly that explicitly breaks the symmetry associated with the axial-vector current $\bar{q}\ I_3\ \gamma_\mu\gamma_5\ q$, and this in turn directly affects the coupling of the π^o to two photons. The predicted anomalous decay amplitude is given by [**?**, **?**]:

$$A_{\gamma\gamma} = \alpha N_c/(3\pi f_\pi) = 2.513 \cdot 10^{-2} GeV^{-1} \tag{1}$$

where N_c is the number of colors in QCD, and $f_\pi = 92.42 \pm 0.25 MeV$ [**?**] is the pion decay constant. The number given above is for the accepted value of $N_c = 3$.

The width of the $\pi^o \to \gamma\gamma$ decay predicted by the anomaly is

$$\Gamma = m_\pi^3 \mid A_{\gamma\gamma} \mid^2 /(64\pi) = 7.725 \pm 0.044 eV, \tag{2}$$

with a 0.6% uncertainty due to the experimental error in f_π. The current experimental value is 7.84 ± 0.56 eV[**?**] and is in good agreement with the predicted value.

The decay amplitude given above is exact in the chiral limit, *i.e.*, when the u- and d-quark masses vanish. In this case, the anomaly is saturated by the π^o pole. However, the real world current-quark masses are of the order of 7 MeV. There are two sources of corrections due to this explicit breaking of chiral symmetry. The first and most important does not change the form of the amplitude given above. It merely replaces the value of f_π in the chiral limit by the measured value determined from π^+ decay[**?**, **?**]. This is a manifestation of the so-called non-renormalization theorem of the anomaly due to Adler and Bardeen. The second correction is due to the mixing of the π^o with the η and the η'. A calculation based on the assumption that the decay constant of the η' is equal to f_π, and on values of the quark mass ratios $(m_u - m_d)/m_s$ and $(m_u - m_d)/(m_u + m_d)$ estimated in several ways, shows that these mixings can add up to 2.5% to the π^o width. A further correction can be induced by terms in the $O(p^6)$ chiral Lagrangian. Such terms would emerge from corrections to the saturation of the anomaly by excited mesons such as the π'. These contributions are suppressed by a factor of m_q/m_{meson}, and would thus be of the order of a few parts per thousand to 1%. Estimates of $O(p^6)$ terms have been done in Nambu-Jona-Lasinio type models[**?**], finding an increase in the π^o width of 0.8% to 1.3%. Thus, an increase of the π^o width of the order of 2 to 3% due to chiral symmetry breaking of the quark masses seems quite likely.

In January 1999, TJNAF PAC15 approved an experiment (E99-XX)(reference) to perform a measurement in Hall B of the π^o lifetime using photoproduction in the Coulomb field of a nucleus. The proposed measurement at the $\simeq$1.4% accuracy level fills this important experimental gap between theory and experiment, and is arguably one of the most fundamental experiments that can be performed with few GeV electrons. New possibilities to measure the analogous decay widths for the η and η', however, will open up with the availability of 11 GeV beams. These are described below.

3.2 Radiative Widths of the η and η' with 11 GeV

3.2.1 Motivation

As with the π^o, the $\eta \to \gamma\gamma$ and $\eta' \to \gamma\gamma$ decays are also dominated by the chiral anomaly. In addition, the relatively large mass of the η' has a subtle effect on the anomaly[?] and there is also the effect of SU(3) breaking which causes π, η, η' mixing[?, ?]. As mentioned previously, this caused a theoretical increase of $\simeq 2\%$ in the π^o width and much larger changes in the η and η' widths[?]. The precise experimental determination of the η and $\eta' \to \gamma\gamma$ widths, leading to a good determination of the $\eta - \eta'$ mixing angle, would have a strong impact on the study of isospin breaking through the $\eta \to \pi\pi\pi$ decay, whose absolute rate is determined using the $\eta \to \gamma\gamma$ width.

3.2.2 Previous Measurments of the η and η' Radiative Widths

The present experimental knowledge of the η meson width is presented in figure 3[?]. Most of the measurements in the figure have been performed using two photon interactions in e^+e^- collisions. One exception is the Cornell measurement of the η width[?] via the Primakoff effect. This gives a width which is significantly lower (at the 3σ level) than those from e^+e^- collisions. Using the same apparatus, the Cornell group measured the $\Gamma(\pi^0 \to \gamma\gamma) = 7.93 \pm 0.39$ eV, in good agreement with the world average value of 7.3 ± 0.2 eV, which is dominated by the collision experiments. As such, the η width should be remeasured by the Primakoff process using state-of-the-art experimental techniques to resolve this discrepancy.

The present status of the η' meson width is presented in figure 4[?]. All the data points are measured through the $e^+e^- \to e^+e^-\gamma^*\gamma^* \to e^+e^-\eta'$ process, and the formation of the η' is identified by measuring its decay particles. As the branching ratios of the η' decay are known at only the $\sim 5\%$ level, the precision of these measurements is limited by these uncertainties. As a result, an alternative approach is strongly desirable. In the next section, we describe a technique in which the η' is tagged by the recoiling nucleus, thus obviating the need to know the branching ratios.

The horizontal lines in figure 3 and figure 4 show the sensitivity of the η and η' two photon decay widths to the $\eta - \eta'$ mixing angle. Venugoapl and Holstein[?] have determined the $\eta - \eta'$ mixing angle by simultaneuosly fitting data from η,η' reactions involving the anomaly $(\eta, \eta' \to \gamma\gamma, \pi^+\pi^-\gamma)$.Their result, $\theta = -20.8^o \pm 3.2^o$, is shown in the figures. It can be seen that the mixing angle is strongly dependent on the widths of η and η'. An improved measurement will provide an important constraint on this parameter. In addition, the figures also indicate that the η and η' two photon decay widths have opposite correspondency to the mixing angle. This would allow one to cross check the experimental systems if one measures

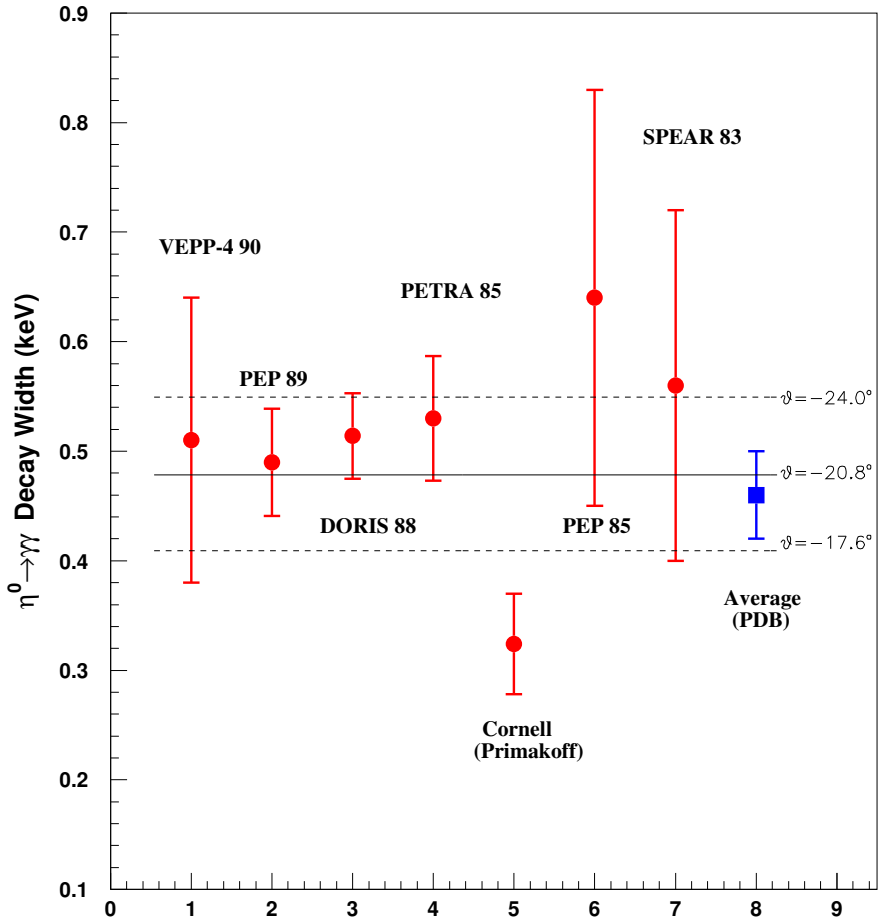

Figure 3: Two-photon decay width for the η meson. Points 1 through 4, as well as 6 and 7 are the results of e^+e^- collisions (for references, see[?]), point 5 is the result of a Primakoff experiment[?]. Point 8 is the Particle Data Book[?] average based on the first five points. The plotted uncertainties combine the statistical and systematic errors in quadrature. The three lines are the widths for different η-η' mixing angles as indicated. See reference[?].

both the η and η' 2γ decay widths.

3.2.3 Measurement of the η and η' Radiative Widths via the Primakoff Effect

We propose to use a nearly real tagged photon beam obtained from 0° degree scattering of 11 GeV electrons to measure the widths of the $\eta, \eta' \to \gamma\gamma$ decays, and to use the very low Q^2 (0.001–0.1 GeV^2) spacelike virtual photons from forward electron scattering to measure the η,η' transition form factors, via the Primakoff effect. The Primakoff effect is shown in figure 5. Mesons are produced by the interaction of a real or virtual photon with a virtual photon from the Coulomb field of the nucleus. The formation of mesons will be identified through missing mass reconstruction by measuring the recoil nucleus. The invariant mass and angle of the η will be reconstructed by detecting the η decay photons from the $\eta \to \gamma\gamma$ reaction.

The production of mesons in the Coulomb field of a nucleus by real photons is essentially the inverse of the decay $\eta, \eta' \to \gamma\gamma$, and the cross section for this process thus provides a

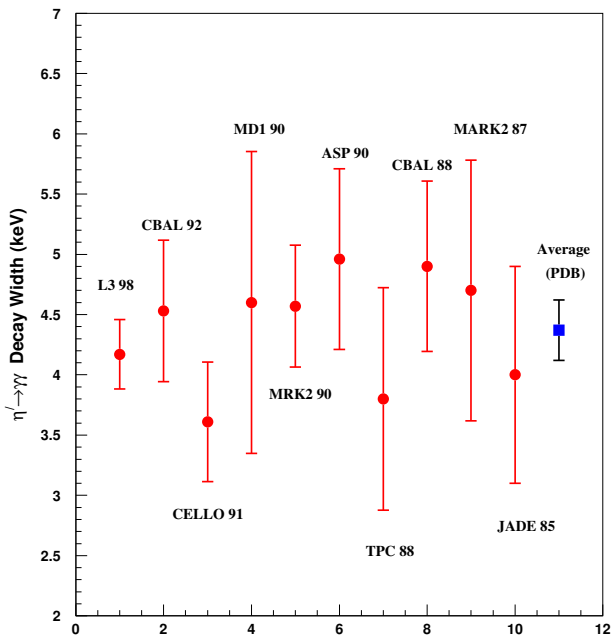

Figure 4: Two photon decay width for the η' meson. All points are the results of e^+e^- collision experiments (for references see[**?**]). The plotted uncertainties combine the statistical and systematic errors in quadrature.

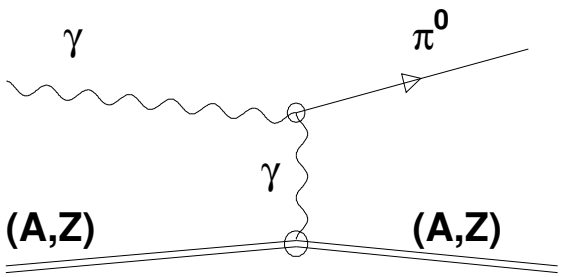

Figure 5: Schematic representation of the Coulomb photoproduction of neutral mesons (Primakoff effect).

measure of the η, η' two-photon decay widths.

For unpolarized photons, the Primakoff cross section is given by[?]:

$$\frac{d^3\sigma_P}{d\Omega} = \Gamma_{\gamma\gamma}\frac{8\alpha Z^2}{m^3}\frac{\beta^3 E^4}{Q^4}|F_{e.m.}(Q)|^2 sin^2\theta_m \tag{3}$$

where $\Gamma_{\gamma\gamma}$ is the decay width of the η or η', Z is the atomic number, m, β, θ_m are the mass, velocity and production angle of the mesons, E is the energy of the incoming photon, Q is the momentum transferred to the nucleus, and $F_{e.m.}(Q)$ is the nuclear electromagnetic form factor, corrected for final state interactions of the outgoing η or η'.

The Primakoff effect is not the only mechanism for meson photoproduction at high energies. There is coherent background from strong production of η,η' in the nuclear hadronic field, and an interference between the strong and Primakoff production amplitudes. The full cross section is given by:

$$\frac{d^3\sigma}{d\Omega_\pi} = \frac{d\sigma_P}{d\Omega} + \frac{d\sigma_C}{d\Omega} + \frac{d\sigma_I}{d\Omega} + 2\cdot\sqrt{\frac{d\sigma_P}{d\Omega}\cdot\frac{d\sigma_C}{d\Omega}}cos(\phi_1+\phi_2) \tag{4}$$

where the Primakoff cross section, $\frac{d\sigma_P}{d\Omega}$, is given by equation (3). The nuclear coherent cross section is given by:

$$\frac{d\sigma_C}{d\Omega} = C\cdot A^2|F_N(Q)|^2 sin^2\theta_\pi \tag{5}$$

and the incoherent cross section is:

$$\frac{d\sigma_I}{d\Omega} = \xi A(1-G(Q))\frac{d\sigma_H}{d\Omega} \tag{6}$$

where A is the nucleon number, $Csin^2\theta_m$ is the square of the isospin and spin independent part of the neutral meson photoproduction amplitude on a single nucleon, $|F_N(Q)|$ is the form factor for the nuclear matter distribution in the nucleus, (corrected for final state

interactions of the outgoing mesons), ξ is the absorption factor of the incoherently produced mesons, $1 - G(Q)$ is a factor which reduces the cross section at small momentum transfer due to the Pauli exclusion principle, and $\frac{d\sigma_H}{d\Omega}$ is the η,η' photoproduction cross section on a single nucleon. The relative phase between the Primakoff and nuclear coherent amplitudes without final state interactions is given by ϕ_1 and the phase shift of the outgoing meson due to final state interactions in the final state is given by ϕ_2.

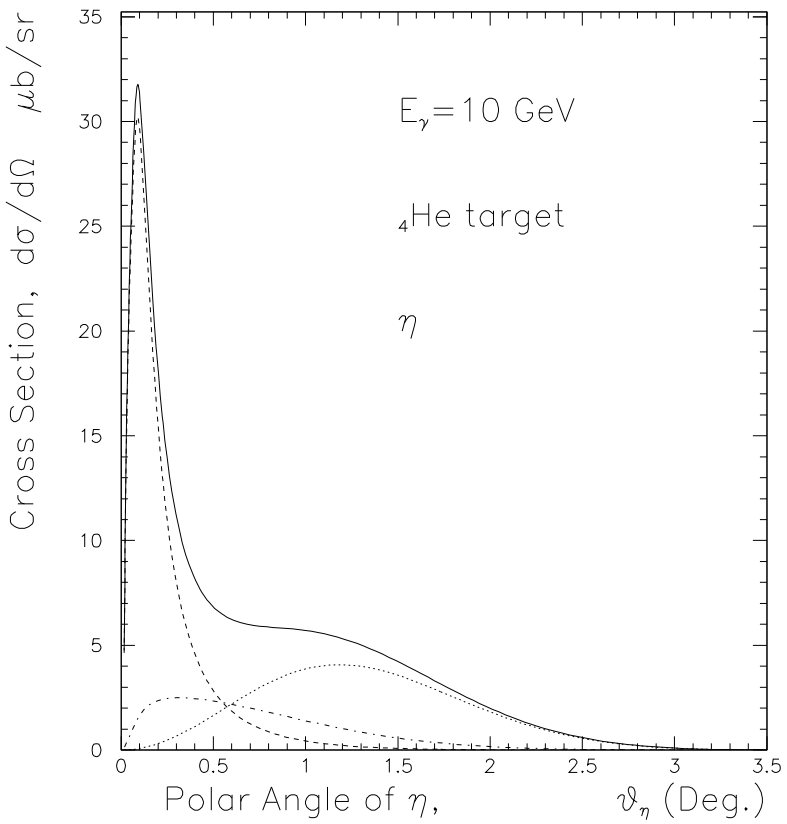

Figure 6: Differential cross sections (electromagnetic and nuclear) for the $\gamma A \to \eta A$ reaction at small angles for ^4He at 10 GeV. The solid line is the total differential cross section from all the process, the dashed line is from Primakoff process, the dot line is from the nucler coherent process, and the dot-dash line is from the interference of the Primakoff and nucler coherent processes.

Kinematical considerations enable one to separate Primakoff from other photo-meson production mechanisms. The Primakoff cross section is zero for mesons emitted along the incident photon direction (minimum four-momentum transfer t to the recoiling nucleus), has a sharp maximum at a very small angle $\theta_m \sim m_\eta(\eta')^2/2E_\eta(\eta')^2$ (small t), and falls rapidly

to zero at larger angles. It is proportional to Z^2, and its peak value is roughly proportional to E^4. The nuclear coherent cross section for spin zero nuclei is also zero in the forward direction, but has a broad maximum outside the angular region of the Primakoff effect, and falls at larger angles as shown in figure 6, where the amplitudes are normalized to the Cornell data[**?**]. The angular dependences (or t dependences) of the Primakoff signal and the background are different, allowing $\Gamma(\eta \to \gamma\gamma)$ and $\Gamma(\eta' \to \gamma\gamma)$ to be extracted from a fit to the angular distribution (or t distribution) of the photoproduced mesons. Measurements of the nuclear effects at larger angles are necessary to determine the unknown parameters in the production mechanism and thus make an empirical determination of the nuclear contribution in the Primakoff peak region. Consequently, to study the η,η' 2γ decay width requires good angular resolution on the meson production angle, or good t resolution on the recoiling nucleus, to eliminate nuclear coherent production background.

Figure 7 shows t, the square of the four-momentum transferred to the nucleus, as a function of the meson production angles for the π^0, η and η'. The arrows indicate the locations of the Primakoff peaks. As one can see, for π^0, the Primakoff cross section is peaked at a very small t ($\sim 10^{-6}\ GeV^2$), so that the recoiling nucleus is likely to stay in the ground state. As the mass of the η and η' are higher than that of the π^0 however, the Primakoff cross sections are peaked at higher t (a few times 10^{-4} for $\eta\ GeV^2$ and 10^{-3} for $\eta'\ GeV^2$). As such, it becomes necessary to check the coherency of the meson production, especially for the case of the η'. A serious drawback of the previous Primakoff experiment[**?**] on $\Gamma(\eta \to \gamma\gamma)$ is that coherency was not established. As a result, recoil detection is required to ensure coherency and thereby distinguish backgrounds. In addition, as indicated in the previous section, in all the existing $\Gamma(\eta' \to \gamma\gamma)$ measurements, the signature of η' production is reconstructed by registering the decay particles from the η'. Consequently, poor knowledge of η' branching ratios will limit the precision of the measurement. By tagging the η' through detection of the recoiling nucleus this uncertainty can be avoided.

As we are going to use the recoil detection technique, the target thickness must be thin enough to allow the recoiling nuclei to exit from the target. For such a thin target, tagging virtual photons at 0° represents a big advantage. With fixed tagging capability, the ratio of the virtual photon rates from zero degree electron scattering and tagged real photon rates is given by [**?**]:

$$\frac{R_{(0^0 e,e'x)}}{R_{(tagged-\gamma,x)}} = \frac{t^V + t/2}{t} \tag{7}$$

where t^V is an effective virtual photon target thickness (~ 0.02), and t is a real photon target thickness. For a $\sim 10^{-5}$ radiation length of target,

$$\frac{R_{(0^0 e,e'x)}}{R_{(tagged-\gamma,x)}} \sim \frac{0.02 + 10^{-5}}{10^{-5}} \sim 10^3 \tag{8}$$

which indicates that the virtual photon rate is about 10^3 times larger than real photon rate. Therefore, we propose using tagged zero degree virtual photons in the $\Gamma(\eta \to \gamma\gamma)$ and $\Gamma(\eta' \to \gamma\gamma)$ measurements.

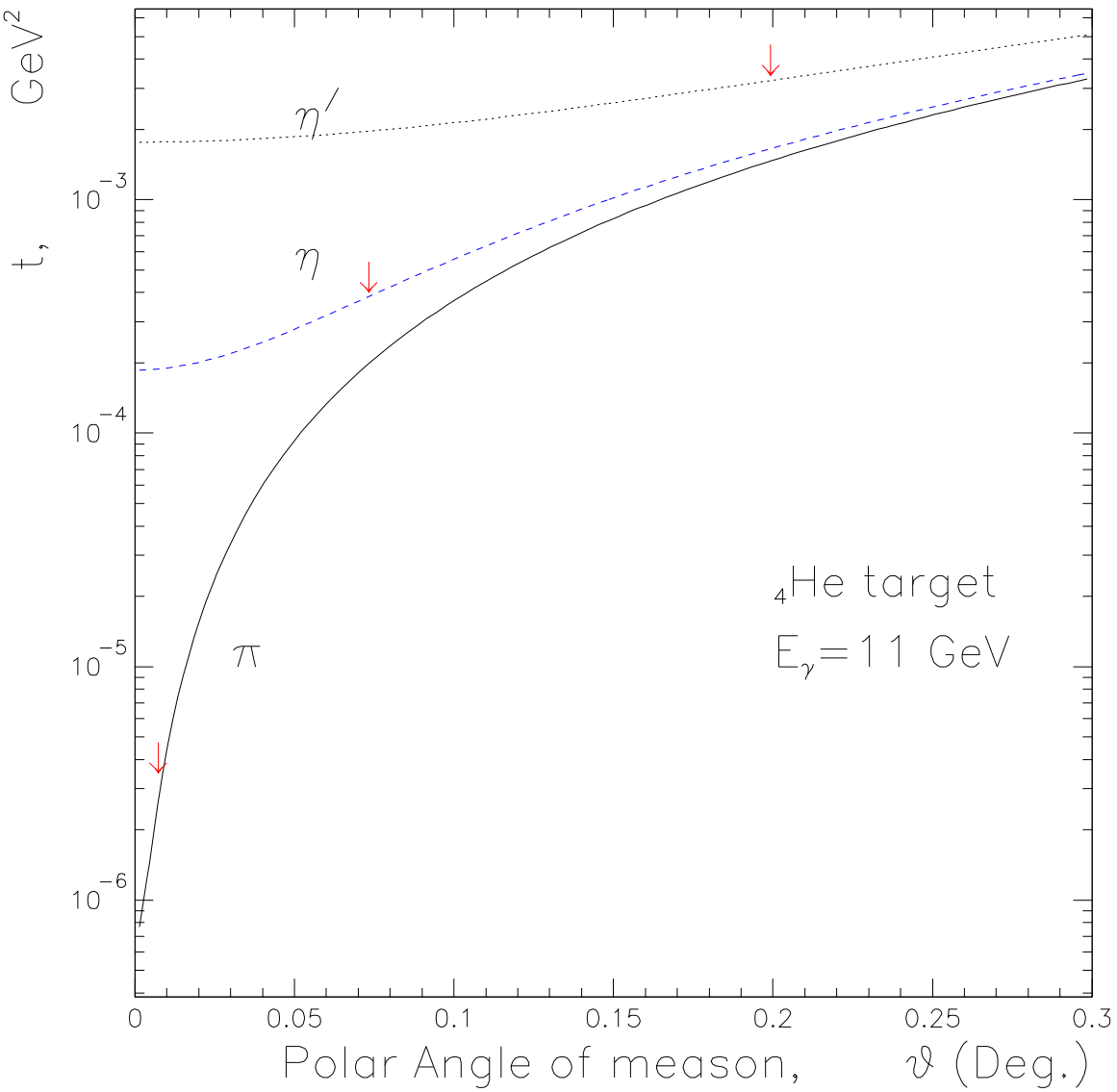

Figure 7: The four-momentum transfer to the nucleus t as a function of the meson production angles of π^0,η and η'. The arrows indicates the location of Primakoff peaks.

The cross sections for the Primakoff effect to produce the η on ^4He is presented in figure 6. Compared to the Primakoff effect to produce the π^0, the η production has a significantly smaller cross section and peaks at larger production angles. This is a consequence of the much larger mass of the η which significantly increases the momentum transfer at a given production angle. As a result the Primakoff peak is harder to distinguish from the nuclear coherent peak. There are two ways to ameliorate this problem. One is to go to higher photon energies. As such, the proposed 11 GeV upgrade to the CEBAF accelerator is vital to these measurements. Another improvement is to use lighter targets such as ^1H, ^4He or ^{12}C. We argue that by simultaneously going to higher photon energies and using lighter Primakoff production targets, one can make clean measurements of the widths.

3.2.4 Experimental Setup for η/η' Width Measurement

We propose to use the virtual photon tagging technique to produce the η/η' mesons, and to detect multiphoton final states in a hybrid calorimeter. In addition to the 11 GeV upgrade to the CEBAF accelerator, such measurements would require (1), a magnetic spectrometer for the virtual photon tagging system, (2), a low energy recoil detector based on low pressure multiwire proportional chambers to enable the separation of photoproduction via the Primakoff mechanism from other processes, and to identify the formation of mesons from missing mass reconstruction, (3) a $1.5m \times 1.5m$ multichannel hybrid calorimeter consisting of lead glass Cherenkov counters and a high resolution insertion in the central region composed of lead tungstate scintillating blocks, and (4), a small angle detector to enable the rejection of Møller and elastically scattered electrons. (see figure 8).

3.2.5 Zero Degree Virtual Photon Tagging System

In order to detect low energy recoiling nuclei from the target, very thin ($\sim 10^{-5}$ radiation length) targets are required. In this case, the virtual photon tagging technique holds a big advantage over real photon tagging. This is because, for the same electron tagging rate, the the ratio of the counting rate between the zero degree virtual photon tagging and tagged real photon is givn by[**?**]

$$\frac{S_{(0^0 e,e'x)}}{S_{(tagged-\gamma,x)}} = \frac{t^V + t/2}{t} \tag{9}$$

where t^V is the effective virtual photon radiator thickness (~ 0.02), and t is the target thickness.

As one can see from the above equations, for $t \ll t^V$, the tagged virtual photons has a higher flux, while maintaining the signal to noise ratio at the same magnitude for the both virtual and real photon cases[**?**]. As pointed out by Hyde-Wright *et. al*[**?**], the signal to noise ratio will be optimized by operating near the bremsstrahlung endpoint, which will be the case in our experiment. The rates of the zero degree virtual photon tagging experiment will be limited by the electron singles rate in the electron spectrometer arm, which is dominated

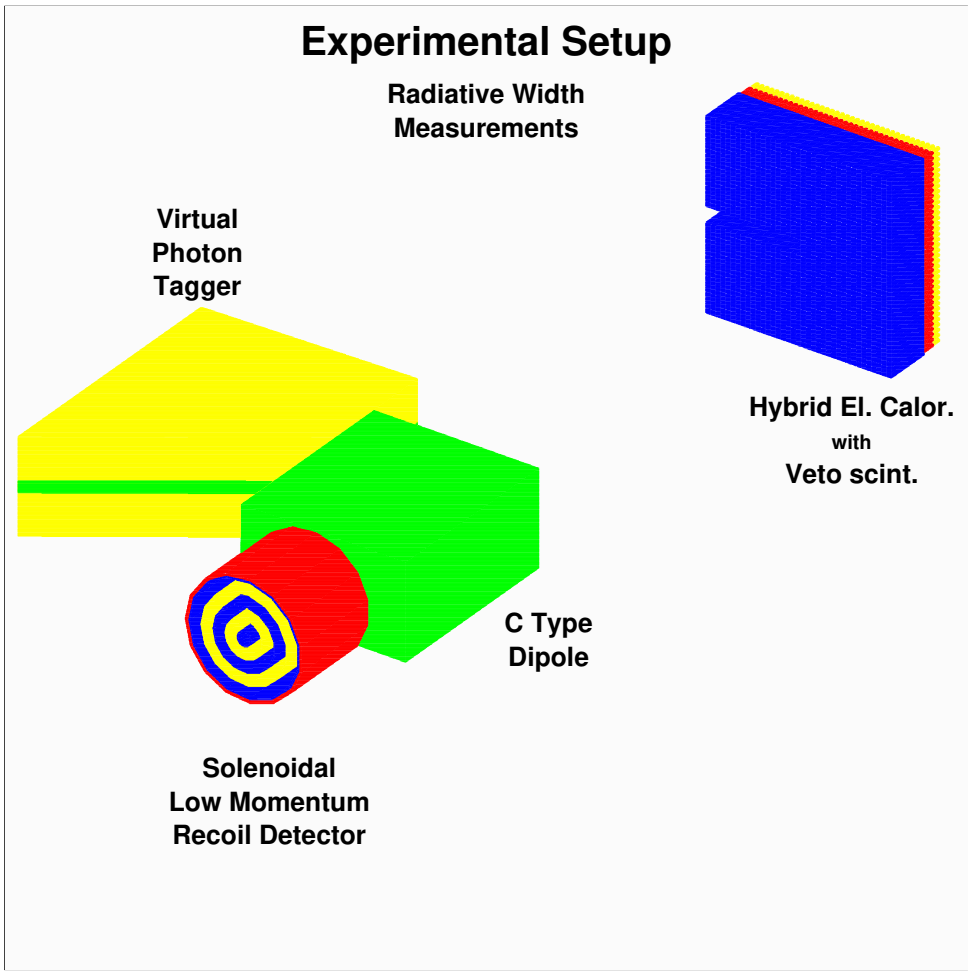
Experimental Setup
Radiative Width
Measurements
Virtual
Photon
Tagger
Hybrid El. Calor.
with
Veto scint.
C Type
Dipole
Solenoidal
Low Momentum
Recoil Detector

Figure 8:

by the electrons from the bremsstrahlung process rather than by the reaction of interest.

The virtual photon flux factor Γ, which is the virtual number of virtual photons radiated per unit photon energy per unit electron solid angle per incident electron is[**?**]:

$$\Gamma(e_1,\omega,\theta)=\frac{\alpha}{4\pi^2\omega}[\frac{e_1^2+e_2^2}{2e_1^2}(\frac{m^2\omega^2}{4e_1^2e_2^2}+sin^2(\frac{\theta}{2}))^{-1}-\frac{e_2m^2\omega^2}{e_14e_1^2e_2^2}(\frac{m^2\omega^2}{4e_1^2e_2^2}+sin^2(\frac{\theta}{2}))^{-2}-\frac{(e_1+e_2)^2}{4e_1^2}(\frac{\omega^2}{4e_1e_2}+sin^2(\frac{\theta}{2}))^{-1}] \tag{10}$$

where e_1 and e_2 are the incident and scattered electron energies, θ is scattering angle, ω is photon energy, m is electron mass.

Integrating over $d\Omega=4\pi dsin^2(\frac{\theta}{2})$:

$$\int_0^{4\pi sin^2(\frac{\theta}{2})}d\Omega=\frac{\alpha}{\pi\omega}[\frac{e_1^2+e_2^2}{2e_1^2}ln(\frac{4e_1^2e_2^2}{m^2\omega^2})+\frac{e_1^2+e_2^2}{2e_1^2}ln(\frac{m^2\omega^2}{4e_1^2e_2^2}+sin^2(\frac{\theta}{2}))-\frac{e_2}{e_1}sin^2(\frac{\theta}{2})(\frac{m^2\omega^2}{4e_1^2e_2^2}+sin^2(\frac{\theta}{2}))^{-1}-\frac{(e_1+e_2 \tag{11}$$

For an 11 GeV electron beam and 10 GeV tagged virtual photons, the flux factor distribution is shown in figure**??**, and the integrated flux as a function of electron scattering angle θ is shown in figure **??**. It can be seen that the virtual photons are mostly in the forward direction, and the intensity of photons falls rapidly with the scattering angle.

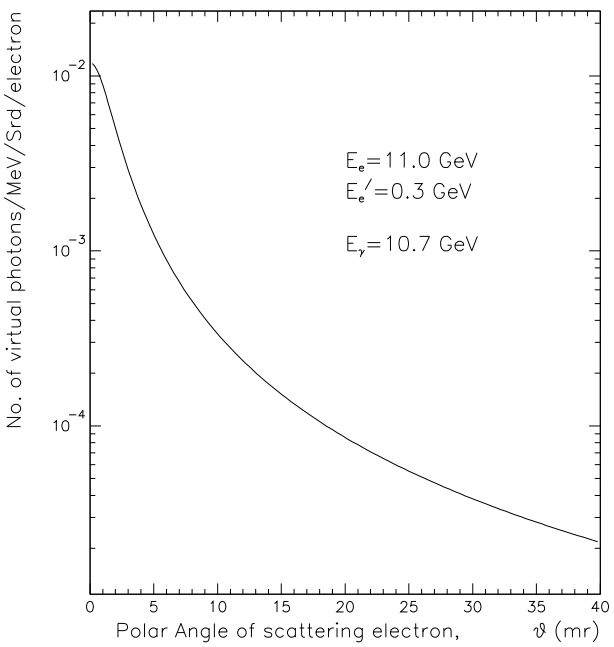

Figure 9: Calculated photon flux factor angular distribution.

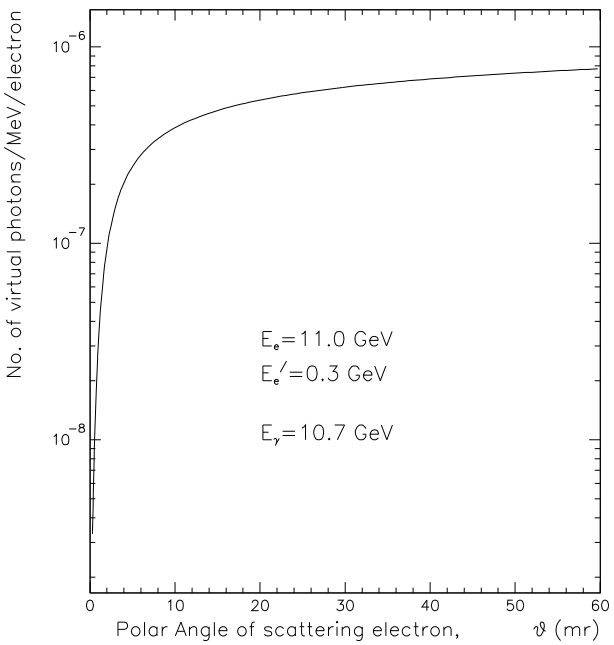

Figure 10: Integrated photon flux via electron scattering angle.

The currently existing zero degree virtual photon tagger, the Enge spectrometer at TJNAF which was used in an HNSS hypernuclear spectroscopy experiment (Mar 1–May 14, 2000), can be used in our experiment with some minor modifications. The spectrometer is a split pole magnet designed by H. Enge[**?**]. The spectrometer parameters are shown in Table3.2.5**??**.

Momentum	240– 360 MeV/c
Design central momentum	276 MeV/c
Total Length	$\sim$ 5 m
Acceptance	
Solid angle acceptance	1.6 msr
Horizontal acceptance	25 mr
Vertical acceptance	20 mr
Momentum bite	$\pm$20%
focal plane dimension	
Length	104 cm
Tilt	42^o
Horizontal	80 cm
Momentum resolution	3×10^{-4}

The focal plane for this spectrometer is located near the back face of the magnetic pole

piece. Resolution without correction for angle-position correlation is about 3×10^{-4}, so that only a focal plane detector package, a silicon strip detector and a segmented scintillator detector, were used during the HNSS experiment for timing and particle identification as well as position. In the Primakoff experiment, we monitor the virtual photon flux by the electron scattering angle. Therefore, another off focal plane detector is needed in order to measure the electron scattering angle. During the HNSS experiment, the Enge spectrometer proved to be capable of running at electron singles rates of up to 1.5×10^8/sec, which is much higher than our requirement ($\sim 7 \times 10^6$).

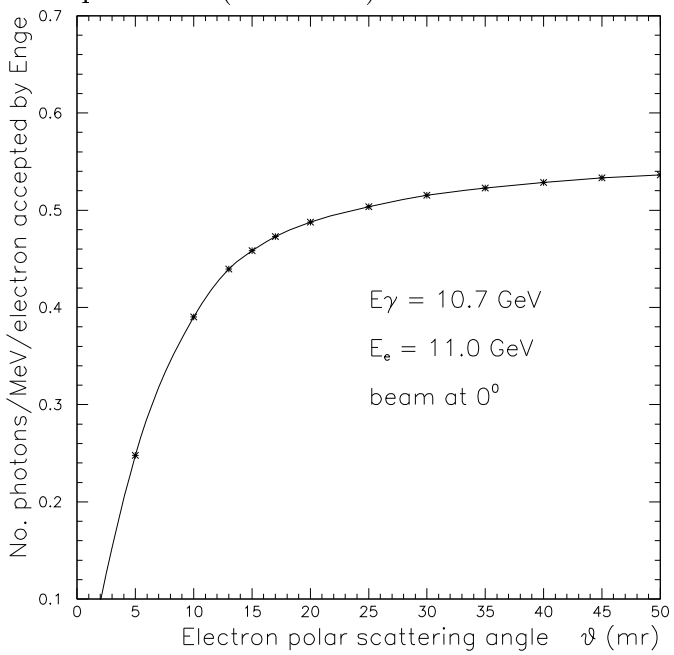

Figure 11: The photon flux distribution registered by Enge acceptance.

Figure 11 shows the photon flux distribution after passing through the Enge spectrometer acceptance, which was simulated by the RAYTRACE [**?**] program. It indicates that we may control the photon flux to better than 1% if the angular resolution is better a few mr.

As the Enge spectrometer angular acceptance is relatively small, we are also keeping open the option to use another electron spectrometer which has a larger acceptance, so that we will be not sensitive to the spectrometer offsets.

3.2.6 Low-Energy Recoil Detection

3.2.7 Importance of Low-Energy Recoil Detection

Detection of recoiling nuclei can offer important kinematical constraints on the reaction. Low-energy recoil measurements in Primakoff experiments performed in conjunction with measurements of the forward system allow one to:

- Separate the coherent process from incoherent background;
- Determine the four-momentum transfer to nucleus (t) with high precision;
- Exclusively identify the formation of the mesons without detecting their decay particles.

A crucial parameter in the Primakoff process is the square of the invariant four-momentum, t, defined as

$$t = (p_o - p_i)^2 = (p_r - p_t)^2 \tag{12}$$

where p_i is the momentum of incident photon, p_o is the momentum of outgoing meson (η or η'), p_t is the momentum of target particle, and p_r is the momentum of the recoil nucleus. Assuming that the target is at rest ($p_t = 0$), in a coherent process ($m_r = m_t = M$), one obtains from the above definition:

$$t = (p_r - p_t)^2 = (E_r - M)^2 = -2MT, \tag{13}$$

where T is recoil nucleus' kinetic energy. Therefore the measurement eror will be determined by:

$$\delta t = 2M \cdot \delta T \tag{14}$$

which shows that error in t is determined only by the uncertainty of T. Comparing this with the measurement of t from the forward angle spectrometer in the elastic process, at small scattering angles θ_o, t can be approximated by

$$-t \sim p_i^2 \cdot \theta_o^2, \tag{15}$$

For a known incident momentum p_i, the error in t is:

$$\delta t \sim 2p_i^2 \cdot \theta_o \cdot \delta\theta_o, \tag{16}$$

As one can see, t is determined by the error in the forward scattering angle, and is also proportional to p_i^2. When the incident momentum p_i increases, the error, δt, grows as well. As a result, determining the t through the recoil measurement has an advantage over measuring the forward scattering angle. As mentioned earlier, the recoil detection technique is also the only way to reach a measurement error of less than 5% in the case of the η' because of the poor knowledge of the η' decay branching ratio ($\sim 5\%$).

As shown in figure12, the kinetic energy of the recoiling nucleus is low and thus a thin target is very important to allow recoiling nuclei to exit the target. Therefore one has to run an intense beam to have a good production rate. As a result, the recoil detectors must have the ability to work in a high radiation environment. The properties of Low-Pressure Multiwire Proportional Chambers (LPMWPCs) and Low-Pressure Multi-Step Chambers (LPMSCs) [2,3] are appropriate to these goals. The main features of such chambers are summarized below:

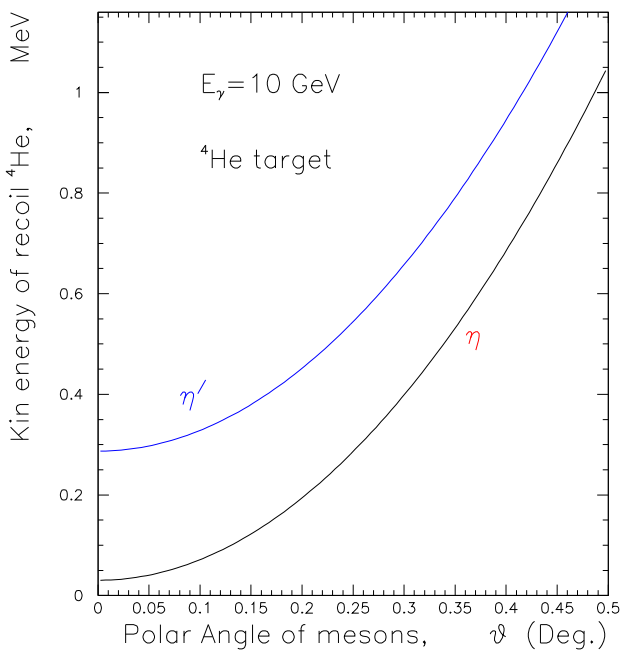

Figure 12: Kinetic energy of recoil ^4He as functions of η and η' production angles.

- High rate capability ($\sim 10^5 Hz/mm^2$);
- Extreme insensitivity to gamma and neutron backgrounds;
- Capability to operate from an external gate, allowing the minimization of space charge effects;
- Negligible radiation damage;
- Good timing resolution ($\sim$ 200 ps, FWHM for fission fragments);

- Good position resolution ($\sim 200\mu m$, FWHM)
- High efficiency ($\sim 100\%$) for detecting low energy recoils;
- Negligible influence on the energy of recoils (the recoiling nucleus travels through the detectors with practically constant velocity).

3.2.8 Scientific Evaluation of the Low Pressure Chamber Technique

During the past four years, a member of our collaboration (A. Margaryan) has been leading a group to develop low-pressure MWPCs for a time-zero fission fragment (FF) detector (Fig.1) for the direct measurement of the heavy hypernuclei lifetime at Jefferson Lab. The detector's characteristics and the method of time-zero reconstruction were investigated using fission fragments from a Cf-252 spontaneous fission source. It is shown that heptane, hexane, and isobutane gases at a pressure of 1-3 Torr are all suitable for such a fission fragment detector. As desired by experiment E95-002 (E99-003) [4], a timing and position resolution of about 200ps (FWHM) and 800μm (FWHM) for a chamber size of $21 \times 21\ cm^2$ was achieved (Fig.2). In order to test the influence of the high radiation on the operation of the fission fragment detector, it was put in Hall C during E96-003 and E91-007 experiments near the beam at 7°, 20 meters downstream from a 4% radiator and a 12 cm liquid deuterium target (Fig.3). There were no noticeable changes in timing resolution of the detectors up to 10μA electron beam current, which produces 10^9 electrons/second in the solid angle of the chamber according to a Monte Carlo simulation [5]. At higher intensities (40-70 μA), the signals decreased 2-3 times due to space charge effects, but the time resolution of fission fragments from a Cf-252 source become worse by only 30% as shown in Fig 6.

Amour's figure 1 and 2

Amour's figure 6.

In February 2000, during the commisioning of the HNSS hypernuclei experiment in Hall C, the chamber was put in front of the electron beam dump. There was no pile up when an approximately 1 μA, 1.8 GeV electron beam was passed directly through the chamber.

Similar techniques have been used for the measurement of the lifetime of heavy hypernuclei with the recoil shadow method and internal targets in the storage ring COSY-Julich [6]. Low pressure MWPCs have been operated at a distance of $\sim$ 30 cm from the target ($\sim 60\ \mu g/cm^2$) with $\sim 10^{10}$ protons at COSY and a cycle time of 10s. This internal target geometry corresponds to an external target experiment with an extracted beam of $\sim 1.6 \mu A$ of 1.9 GeV protons.

The low-pressure technique has also been utilized to measure absolute electrofission and photofission cross sections [7,8]. In this case, the detectors were operated at a distance of $\sim$ 20 cm from the targets ($\sim 500 \mu g/cm^2$) at peak electron currents of $\sim$ 10 mA (average currents were $\sim 0.5 \mu A$)[8] or when a bremsstrahlung photon beam with intensity $10^9 - 10^{10}$ photon/sec passed directly through the detector with 30 mg/cm^2 Al plus 1.0 mg/cm^2 U target inside [8].

A large area detection system which consists of twelve low-pressure MWPCs was used in the search for exotic super-massive nuclei [9]. Stable detector operation was reached even at the highest beam intensities, with electron currents in the detectors of at most 5 μA.

By means of this low-pressure technique it is possible to detect:

- Protons with energy 0.1– 5 MeV;
- Deutrons with energy 0.2–10 MeV;
- Alpha particles with energy 0.4 – 100 MeV;

as well as more heavy particles.

Coherent π^o electroproduction on ^4He was studied using the internal target facility of the AmPS electron storage ring at NIKHEF [10-11]. The experiment was performed at a luminosity of about $10^{33} cm^{-2}/s$ with a stored beam of about 200 mA (615 MeV and 676 MeV) electrons and a ^4He and ^2H gas target of 10^{15} atoms/cm^2. The neutral pions were detected by the coincidence of the scattered electrons with the recoiling ^4He nuclei measured by a dedicated recoil detector [11]. This detector was designed to detect light ($A \leq 4$), low-energy (0.5–24 MeV for proton and 1–95 MeV for ^4He) nuclei. It consisted of four successive layers: a low-pressure (isobutane at 3 mbar) two-step MWPC, two layers of silicon strip detectors and a 5 mm thick scintillator.

As such, we conclude that the recoil detectors based on low-pressure MWPCs can be operated at a luminosity up to $10^{33}\ cm^{-2}/s$.

3.2.9 Low Energy Recoil detector based on LPMWPCs

The gas-filled magnetic spectrometer separator has been widely exploited in experimental nuclear physics [12-14]. This technique is suitable for the detection and identification of low-energy recoils. If a charged heavy particle moves in matter, its ionic charge is changed by charge changing collisions. These processes occur in the gas along the trajectory of

the particles in a magnetic field. The deflection in the magnetic field will be inversely proportional to the q_{ave} – the average of all charge values of the ion along its path in the magnetic field. When the magnetic field region contains gas at several torr pressure, the spread of the q_{ave} of the ions along their paths as they are deflected in the magnetic field becomes much smaller than the spread of the q_{ave} in the case in which the ions are deflected in vacuum, as shown schematically in Fig.7a,b. We suggest to use low-pressure heptane and hexane as a gas environment in the magnetic spectrometer-separator and as a working gas for the LPMWPCs or LPMSCs simultaneously. By means of the low-pressure technique, the time-of-flight and position parameters of the low energy recoils can be determined within a few hundred picoseconds and a few hundred micrometer precision, and consequently one can determine their velocities and magnetic rigidities within a precision of a few percent. In addition, the dE/dx of low energy recoils can be measured. In a magnetic field B, an ion has a mass of A_1, ionic charge q and velocity v. The trajectory of the ion is determined in the magnetic field by the Lorentz force. If B and v are perpendicular, the magnetic rigidity in units of Tesla-meters is given by the following equation:

$$BR = 0.0227 A_1 \cdot (v/v_0) \cdot /q_{ave}(Z_1, Z_2, v, p) \tag{17}$$

where the ion velocity is in units of the Bohr velocity $v_0 = 2.19 \times 10^6$ m/s, and the mean ionic charge q_{ave} depends on the atomic number Z_1 of the deflected ion and its velocity and approximately $q_{ave} \propto Z_1^{0.6}$. Furthermore, the mean ionic charge q_{ave} depends on the gas density which is represented by the pressure p, and the atomic number Z_2 of the matter in which the ion is moving. The total deflection in the field is proportional to the mean value of q/v averaged over the whole path length in the field. On the other hand, the magnetic rigidity of the ions only depends on the mass and atomic number of the ion, $BR = f(A_1, Z_1)$, if their velocity is known and they are moving in a constant density gas with known atomic number. A separator thus may be calibrated with isotopes of known A_1 and Z_1. For example, monoenergetic, isotopically pure recoils from electron nucleus elastic scattering can be used to calibrate a gas-filled separator. The resolving power of the gas-filled separator may be written as:

$$(A_1/\delta A_1)_{fwhm} = 100/(\delta(BR)/BR)_{fwhm}, \tag{18}$$

with $\delta(BR)/BR)_{fwhm}$ in %. For a 2% total BR resolution,

$$(A_1/\delta A_1)_{fwhm} = 50; (Z_1/\delta Z_1)_{fwhm} = 30. \tag{19}$$

Such a device will have wide application in intense electron beam experiments, providing the detection and identification of low-energy recoil nuclei in a wide range of mass and charges.

In the Primakoff process with a beam energy $\sim$ 11 GeV, the recoil kinetic energy is very low ($T_{min} \sim 0.5$ MeV). The deposited energy of the recoil particles in the detector is comparable to the energy of recoils:

$$(dE/dx) \times \delta x \sim T \tag{20}$$

Thus the recoils can be identified by the measurement of the velocities V_1 and V_2, before and after the energy deposition:

$$A \times V_2^2/2 = A \times V_1^2/2 - (dE/dx) \times \delta x \tag{21}$$

and

$$A = \frac{2 \times (dE/dx) \times \delta x}{V_1^2 - V_2^2} \tag{22}$$

In Figure 8 we have plotted the FWHM of the energy loss of the alpha after passage through different path lengths in argon. The solid line is the experimental data from [15], the points are the results of the simulation using our Monte Carlo code [3]. One can see that the dispersion of the fluctuations of $(dE/dx) \times \delta x$, and consequently V_2, are about 2% and that the MC code described the experimental results within few percent precision. In figure 9 we present the FWHM of the energy loss fluctuations $(dE/dx) \times \delta x$ of ~ 6 MeV carbon nuclei in argon obtained from our Monte Carlo code. One can see that for heavy recoils the fluctuations are even less. On the other hand, the precision of the velocity measurement using the low-pressure technique is $\sim 1\%$. Therefore in low energy recoil detection, particle identification can be done by the velocity measurement only. The resolving power for A and Z in this case is about the same as for the gas-filled separator ($(A_1/\delta A_1)_{fwhm} = 50$, $(Z_1/\delta Z_1)_{fwhm} = 30$).

Figure13 shows the range of the recoil ^4He and ^{12}C in a 1 Torr pressure Heptane gas for different kinetic energy. At ~ 0.2 MeV kinetic energy, the range of ^4He is ~ 35 cm and ^{12}C is ~ 15 cm, which indicates that the recoil nuclei in such energy range can travel enough distance to reach the detector.

We have a preliminary conceptual design of the recoil solenoid detector. It may consist of the following three elements: (1), a solenoid magnet; (2) the 3–5 internal layers of Low Pressure Multiwire Proportional Chambers (LPMWPCs) to detect the very low energy of the recoil nuclei; (3), a solid state detector in the outer layers (silicon strip detector or segmented scintillator detector) for the higher energy recoil particles. Further research on this recoil detector is planned.

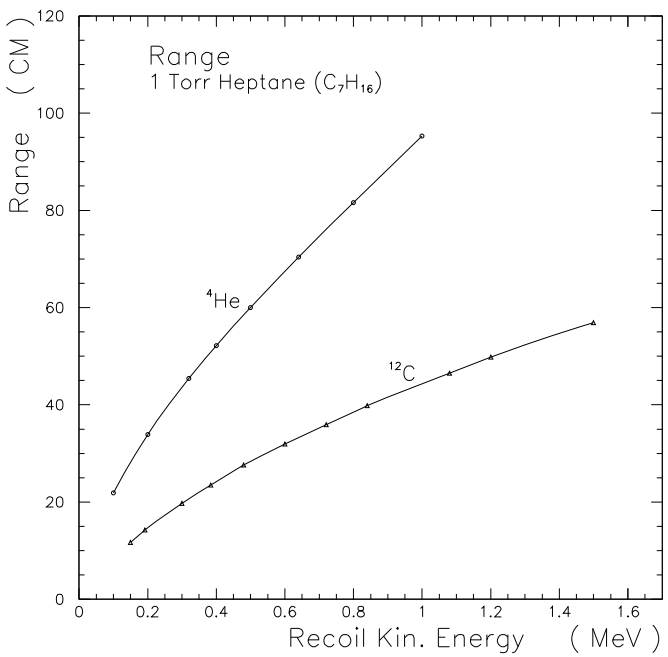

Figure 13: Range of ^4He and ^{12}C in Heptane for different kinetic energy.

Amour's fig 7a,b

Amour's fig 7a,b

figure 8

figure 9

3.2.10 The Hybrid Calorimeter (HYCAL)

The electromagnetic decay particles from eta and eta', and scattering electrons in the transition form factor measurement will be detected in the highly segmented array of Hybrid Shower Calorimeter (HYCAL) located at the downstream of the target. Currently our collaboration (primEx) is constructing a Hybrid Shower Calorimeter for an approved pi^0 life time experiment in Hall B. This shower counter will be used in the proposed experiment with slightly larger size. It is about 150.0 x 150.0 cm^2 in the dimension transverse to the beam. The calorimeter is designed to measure both the position and the energy of electromagnetic showers using a two dimensional matrix of radiators (lead glass and crystals). That will be accomplished by choosing the cross section of the individual counters small enough so that the energy leakage into adjacent counters can be used to determine the position of the shower axis. The calorimeter will consist of two types of detectors. The outer part of the calorimeter will be made from lead glass Cherenkov detectors with the size of the radiators 4.0x4.0x40.0 cm^3. For enhanced position and energy resolution to measure the mass and angle of the small angle, the central region of the HYCAL will be constructed from lead tungstate ($PbWO_4$) crystals of size $2.125 \times 2.125 \times 21.2 cm^3$. These high resolution detectors will cover a $46.75 \times 46.75 cm^2$ region around the beam where at least one photon from the $\eta \to \gamma\gamma$ decay will hit the calorimeter. In addition, this crystal insertion will significantly improve the radiation hardness of the detector near the beam line where radiation doses can be high. The central $12 \times 12 cm^2$ hole will be left open to enable the photon beam to pass through. The modules contiguous with this region on the beam axis as well as the two outermost layers of modules in the lead glass wall will be excluded from the fiducial volume of the detector to control coordinate resolution and detection efficiency near the boundaries of the detector. To monitor and correct possible gain changes due to temperature and aging, a light monitoring system will be used.

3.2.11 Lead Glass Detectors

We will use Cherenkov counters composed of TF-1 type lead glass radiator of dimensions $4.0 \times 4.0 \times 40$ cm^3. Their physical properties are listed in the table 1. The lead glass block dimensions are optimized to measure photon energies in the region from a few hundred MeV to a few GeV where light collection and photon statistics are defining the energy resolution, and energy leakage is relatively unimportant. Also, the lead glass radiators provide a good compromise between the requirements for precision of position and energy measurements and the complexity and price of the entire calorimeter. Cherenkov light produced in the lead glass radiator(1) from the electromagnetic shower will be detected by a photomultiplier tube (PMT)(5) of the FEU-84 type made in Russia. The individual blocks will be wrapped in aluminized mylar foil (2) (25 μm) as a light reflector and thick ($50 \mu m$) black paper (3) for optical isolation between the blocks. Electromagnetic calorimeters based on this type of lead glass and PMT's are widely used in many high and medium energy experiments[**?**][**?**]. The excellent optical transparency and optimized transverse size of the lead glass radiator provide good energy and position resolutions:

PbO content (wt perc)	50.8
density (g/cm^3)	3.85
Radiation length	2.7
Critical energy (MeV)	17.5
Refractive index	1.65
Nucl. collis. length (cm)	21.8
Coefficient of thermal expansion ($\times 10^{-7}$ cm/cm/C)	88

Table 1: Physical properties of the Russian made TF1 lead glass modules.

$$\frac{\sigma_E}{E}(\%) = \frac{4.}{\sqrt{E}} + 2.5, \sigma_x = \frac{5mm}{\sqrt{E}}, \tag{23}$$

where E is in GeV.

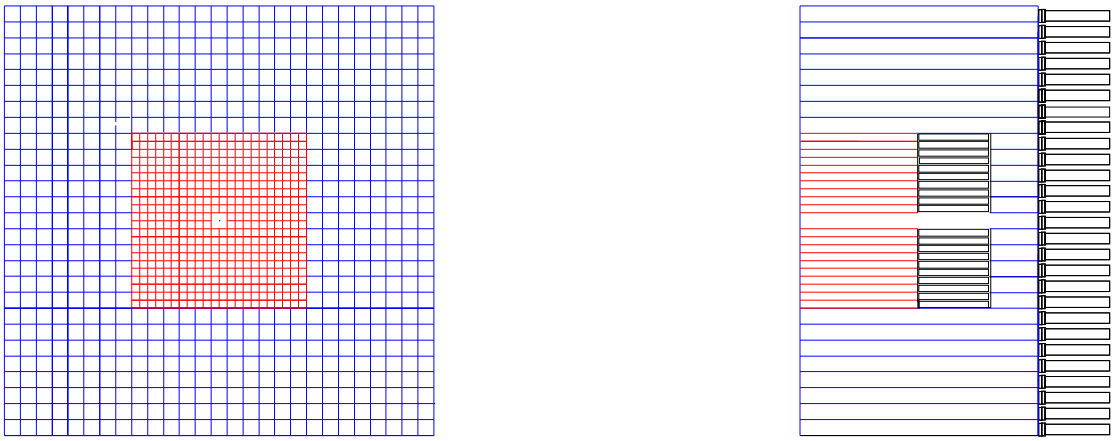

a) Front view b) Side view

Figure 14: The schematic structure of the HYCAL calorimeter.

3.2.12 Lead Tungstate Detectors

As the Primakoff cross section peaks at extremely small angles: $\theta_\eta = 0.1^o$ at $E_\gamma = 10$GeV, in order to identify and extract the Primakoff amplitude (at very small recoil energy range, the formation of eta will be determined by $\eta \to \gamma\gamma$ detection), the experimental setup must have sufficient resolution for the η production angle. This resolution depends strongly on the decay photon energy and position accuracy of the calorimeter. The high resolution insertion to the HYCAL detector will improve the angular resolution by 50%. We plan to use 480 finely granulated lead tungstate ($PbWO_4$) scintillating crystals in the central part of the

Radiation length (cm)	0.89
density (g/cm^3)	8.28
Moliere radius (cm)	2.0
Peak wavelength (nm)	450-500
Index of refraction	2.2
Temp. dep. of light yield ($\%/^\circ C$)	-1.9

Table 2: Physical properties of the lead tungstate crystals.

calorimeter. Their properties are shown in table **??**. The transverse size of the crystals will be $2.125\times2.125cm^2$, and the length will be selected between 16-20 cm (18-22 X_o) after performing beam tests of the prototype detectors. Each crystal will be wrapped in thin aluminum foil and viewed with a Phillips XP1911 PMT coupled to the crystal with optical compound. The light yield of the crystal is highly temperature dependent ($\sim 2\%/^oC$). Therefore, the temperature of the calorimeter has to be well stabilized ($\pm 0.1^oC$). For that purpose all four sides of the calorimeter will be surrounded by water cooled copper plates and thermal isolation. The temperature will be continuously monitored by sensors coupled to the front of the crystals.

The Mainz group recently reported excellent energy resolution with similar crystals operated at a stabilized temperature of 8°C. They found

$$\frac{\sigma_E}{E}(\%) = \frac{1.54}{\sqrt{E}} + 0.3, \tag{24}$$

where E is given in GeV[**?**].

3.2.13 Background Veto Detector

The main source of background in the recoil detector arises from the recoiling nuclei from elastic electron scattering in the target, and the main background in hybrid calorimeter is the Møller electrons. Offline, we will be able to distinguish the recoil events from η and η' production, which are of interest, from the elastic background. This is because their kinematics are very different. As shown in figure 15 and 16, the elastic recoil angle is located near 90^0, while the meson's production angle is smaller. The Primakoff cross section is peaked at a recoil angle of around 40°. On the other hand, the Møller events are also kinematically different from the η and η' decay events in the calorimeter. The Møller events consist of two charged electrons with total energy equaling that of the beam energy, while the η and η' decay events are usually accompanied by at least one γ. This allows one to separate them offline. Online, we will use a background veto detector to cut down both elastic and Møller background at the trigger level. (see figure 17). In addition, the prescaled elastic events can also be used to calibrate the recoil detector and monitor the luminosity.

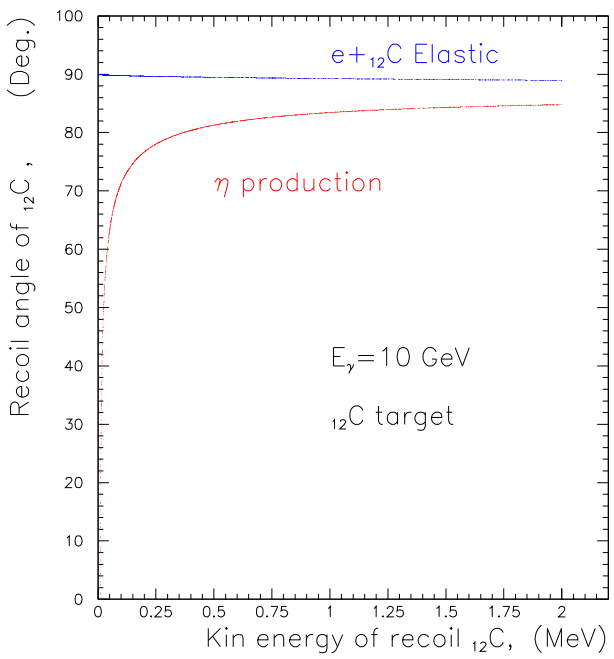

Figure 15: Kinematics of recoil ^{12}C from η production reaction and elastic scattering.

We estimate the rates by assuming a 1μA electron beam ($N_e \sim 6.26 \times 10^{12}$ electron/sec), impinging upon a 40 cm heptane (C_7H_{16}) gas target at 1 torr, which corresponds to $N_{^{12}C} \sim 10^{19}\ atoms/cm^2$. The elastic scatttering cross section is:

$$\sigma_{el} = \int_{0.02MeV}^{\infty} \frac{d\sigma}{dT}(e,^{12}C)dT \sim 6.0mbarn \tag{25}$$

Therefore, the total elastic background rate from ^{12}C is:

$$\begin{aligned} N_{elastic} &= N_e \cdot N_{^{12}C} \cdot \sigma_{el} && (26)\\ &= 6.25 \times 10^{12} \times 10^{19} \times 6 \times 10^{-27} && (27)\\ &\sim 4. \times 10^5 Hz && (28) \end{aligned}$$

On the other hand, for a $150cm \times 150cm$ hybrid calorimeter with $12cm \times 12cm$ central hole to allow the beam to pass through, located ~ 5 meters downstream from the target, the Møller electron background rate on the calorimeter is ~ 67 kHz. In order to veto both elastic and Møller background at the trigger level, we will build a background veto detector,

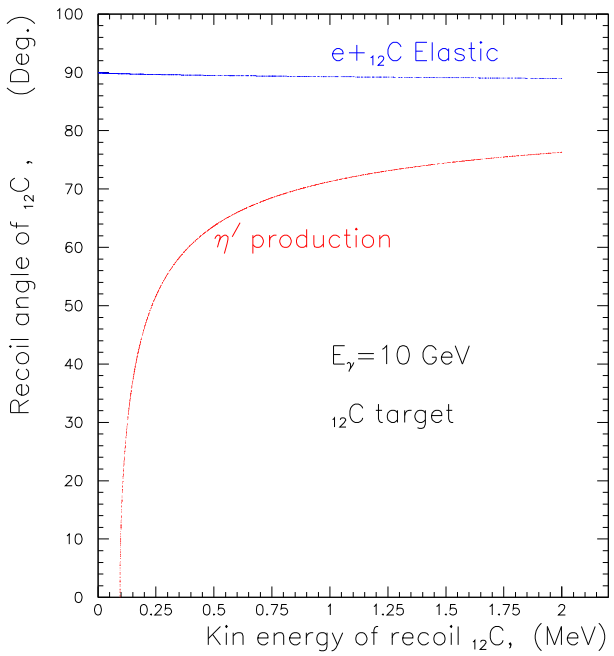

Figure 16: Kinematics of recoil ^{12}C from η' production reaction and elastics scattering.

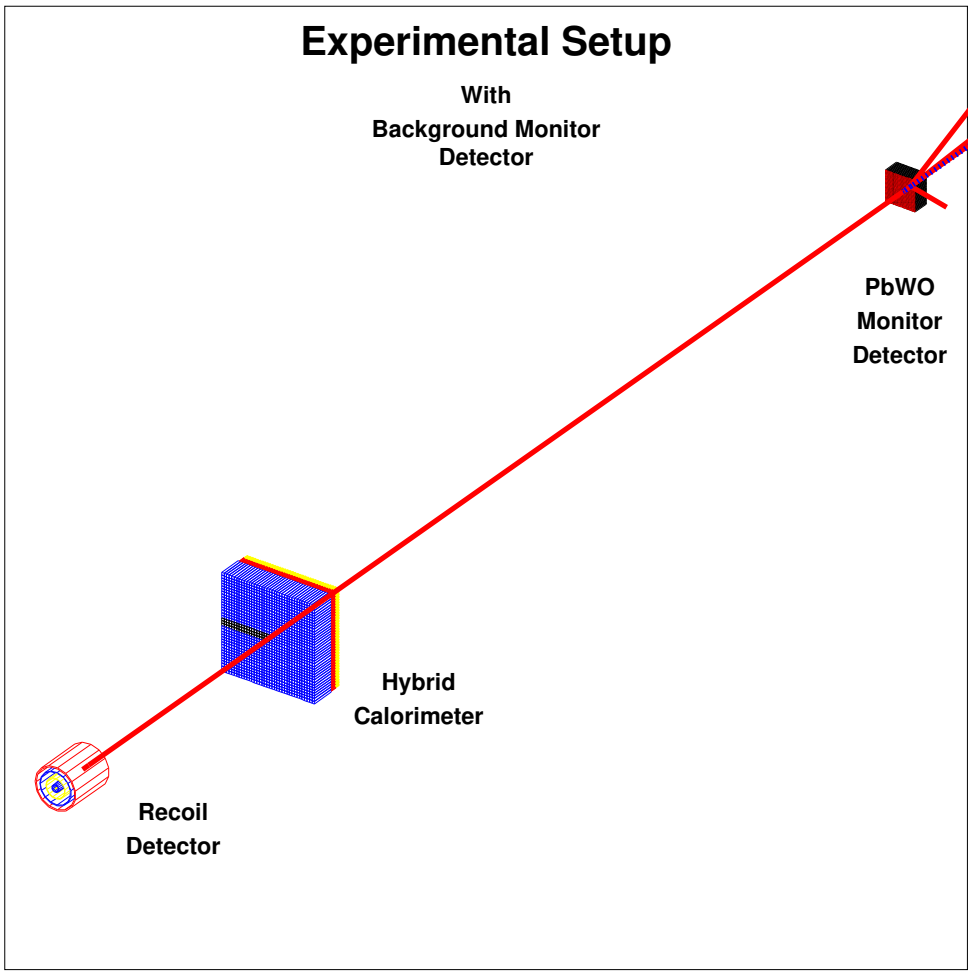
Experimental Setup
With
Background Monitor
Detector
PbWO
Monitor
Detector
Hybrid
Calorimeter
Recoil
Detector

Figure 17:

located ~ 20 meters downstream of the target. It will be about $50 \times 50\ cm^2$ in the dimension transverse to the beam, with a $4 \times 4 cm^2$ hole in the middle. The detector will be constructed from lead tungstate ($PbWO_4$) cystals of size $2.125 \times 2.125 \times 21.2 cm^3$.

Figure 19 shows the Monte Carlo result from a total of 22,000 elastic (e,^{12}C) events. In the figure, (a) shows the elastic electron hit distribution on the hybrid calorimeter without any cut with 44 out of 22000 total events, which means the elastic background will have a very small effect on the calorimeter because of the small electron scattering angle; Figure (c) shows the elastic electrons hitting the background veto monitor detector, with 19956 out of 22000 events; Figure (b) shows the kinetic energy spectrum of recoiling ^{12}C nuclei from elastic scattering before the veto monitor cut, which indicates that the recoil background from the elastic scattering is mostly at small recoil energy. Figure (d) shows the kinetic energy spectrum of the recoiling ^{12}C nuclei from elastic scattering after the veto monitor cut, with only 44 out of 22000 events left. Therefore, the elastic background in the recoil detector is reduced 2×10^{-3} times by the veto monitor. For a 1μA electron beam, we will have a $4 \times 10^5 \times 2 \times 10^{-3} \sim 800 Hz/\mu A$ elastic background left in the recoil detector and the calorimeter after the cut, and the elastic rate on the veto monitor is about 400 KHz per μA electron beam current.

Figure **??** shows the Monte Carlo result simulated from a total of 20,000 Møller events. In the figure, (a) and (c) show the position distribution and energy spectrum of Møller electrons hitting the hybrid calorimeter before the veto monitor cut, and the total hits on the detector is 13512; (b) and (d) show the position distribution and energy spectrum of Møller electrons on the hybrid calorimeter after the veto monitor detector cut, about 395 events left comparing with before the cut, and (d) also indicates that only very small energy Møller events can survive from the veto detector cut, which can be cut eventually by setting detector energy threshold to about 1 GeV.

According to the cross section, the Møller event rate is about 10^5 Hz per 1μA electron beam. Thus, without a veto monitor cut, the Møller event rate on the calorimeter will be:

$$N_m \sim 1. \times 10^5 \times \frac{13500}{20 \times 10^3} \tag{29}$$

$$\sim 67.5 \times 10^3 electron/sec. \tag{30}$$

When adding the veto monitor cut, the Møller event rate will be reduced to:

$$N'_m \sim 1. \times 10^5 \times \frac{400}{20 \times 10^3} \tag{31}$$

$$\sim 2 \times 10^3 electron/sec \tag{32}$$

The Møller event rate on veto monitor detector is $\sim 2 \times 10^5$ electron/sec.

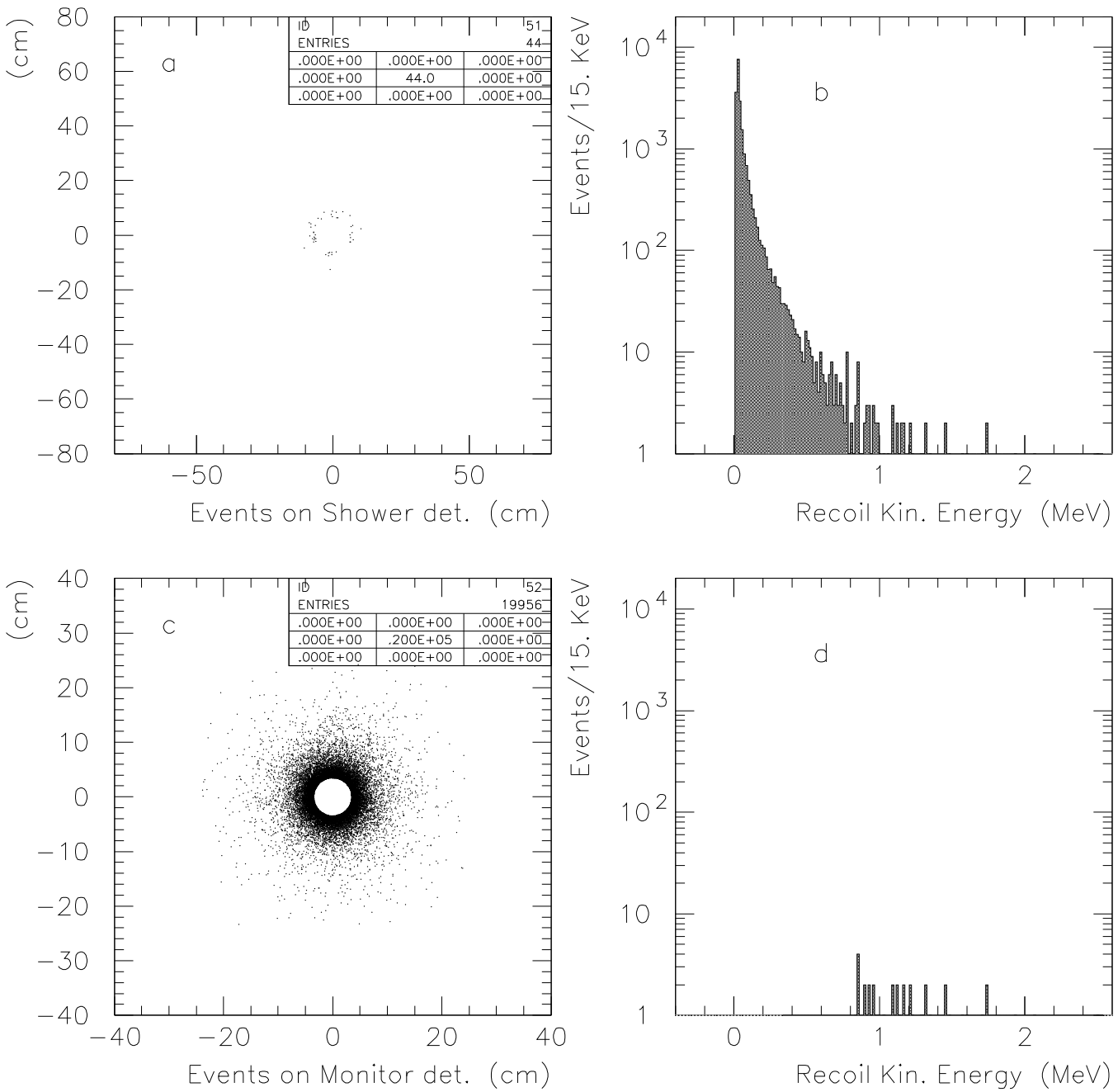

Figure 18: Monte Carlo simulation for $(e,^{12}C)$ elastic background

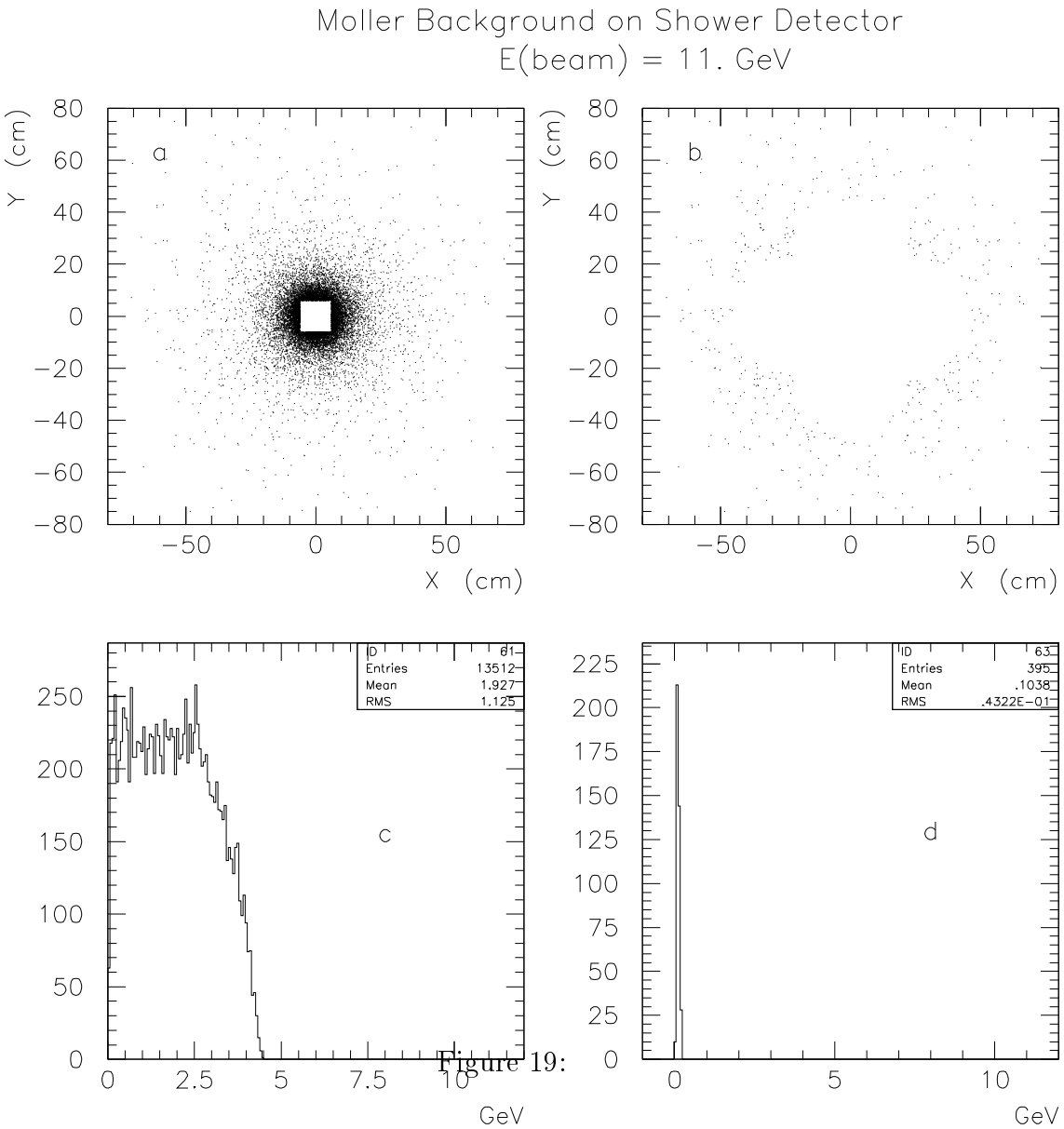
Moller Background on Shower Detector
E(beam) = 11. GeV
a
b
c
d
Y (cm)
X (cm)
GeV
ID 61
Entries 13512
Mean 1.927
RMS 1.125
ID 63
Entries 395
Mean .1038
RMS .4322E-01

Figure 19:

In summary, implementing the background veto monitor detector will greatly help to reduce both elastic and Møller background in the recoil detector and the calorimeter.

3.2.14 Rates and Uncertainties

One can ensure a clean separation of the Primakoff mechanism from background photoproduction processes by exploiting the known Primakoff cross section's energy, Z^2, and angular dependence. As such, we propose measurements on differnent nuclei (^4He and ^{12}C discussed here), a range of energies, and over a range of angles as determined by the hybrid calorimeter (HYCAL).

Figure 20 shows a Monte Carlo simulation of the expected experimentally measured angular distribution of $\eta \to \gamma\gamma$ events on ^4He, where the resolution and geometrical acceptance of the hybrid calorimeter were taken into account. The target thickness was taken to be 2×10^{19} helium atoms/cm^2 and the calorimeter is $1.5m \times 1.5m$ and is 5 meters downstream of the target. The simulation corresponds to 30 days of beamtime at $5\mu Amps$, and yields 20,500 $\gamma\gamma$ events. A fit to these data results in a $\Gamma^{\eta}_{\gamma\gamma} = 0.4603$keV with a 1.8% statistical error. In comparison, the data were generated using the value from the Particle Data Book of 0.463 keV.

A Monte Carlo simulation of η production on ^{12}C was also performed (see figure21) assuming a target thickness of 2×10^{19} carbon atoms/cm^2 where the carbon atoms are in the form of the heptane wire chamber gas. As with the previous simulation, the calculation corresponds to $5\mu Amps$ of beam current for 30 days. It is worth noting, however, that with the proposed setup involving recoil detection with low pressure multiwire proportional counters, the helium and carbon data would be obtained simultaneously. The simulation yields 72,500 $\eta \to \gamma\gamma$ events and gives a 0.7% statistical error on the width.

4 Measurements of the Transition Form Factors $F_{\gamma\gamma^*P}$

Studies of the $\gamma\gamma^*P$ vertex, where P represents the π^o, η, or η' pseudoscalar mesons and γ^* is a virtual photon of low or moderate Q^2, enable one to study the transition regime from soft nonperturbative physics to the hard processes of perturbative QCD. We propose to measure the photon momentum dependence of the form factors $F_{\gamma\gamma^*P}(Q^2)$ and thereby map out an extension to the axial anomaly to provide a clean test of QCD predictions for exclusive processes.

The structure of the meson's electromagnetic coupling is typically parameterized in the context of the vector meson dominance model in which a photon couples to hadronic matter via an intermediate vector meson. Such a model implies a form factor of the form:

$$F_\pi = \frac{1}{1 + q^2_\mu / m_V}, \tag{33}$$

where m_V is the mass of the vector meson. For the charged pion case, the Coulomb form factor has been measured[**?**] and the charge radius was determined to be about 0.6 fm. Due

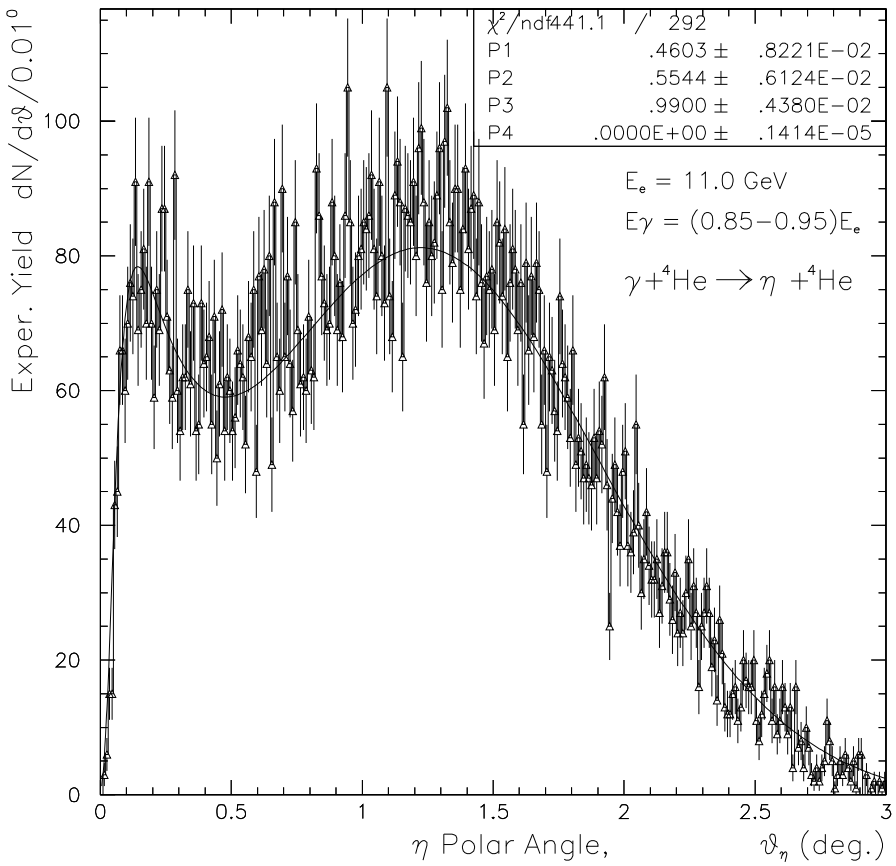

Figure 20: Monte Carlo simulation of experimentally measured angular distribution of $\eta\gamma\gamma$ events on ^4He.

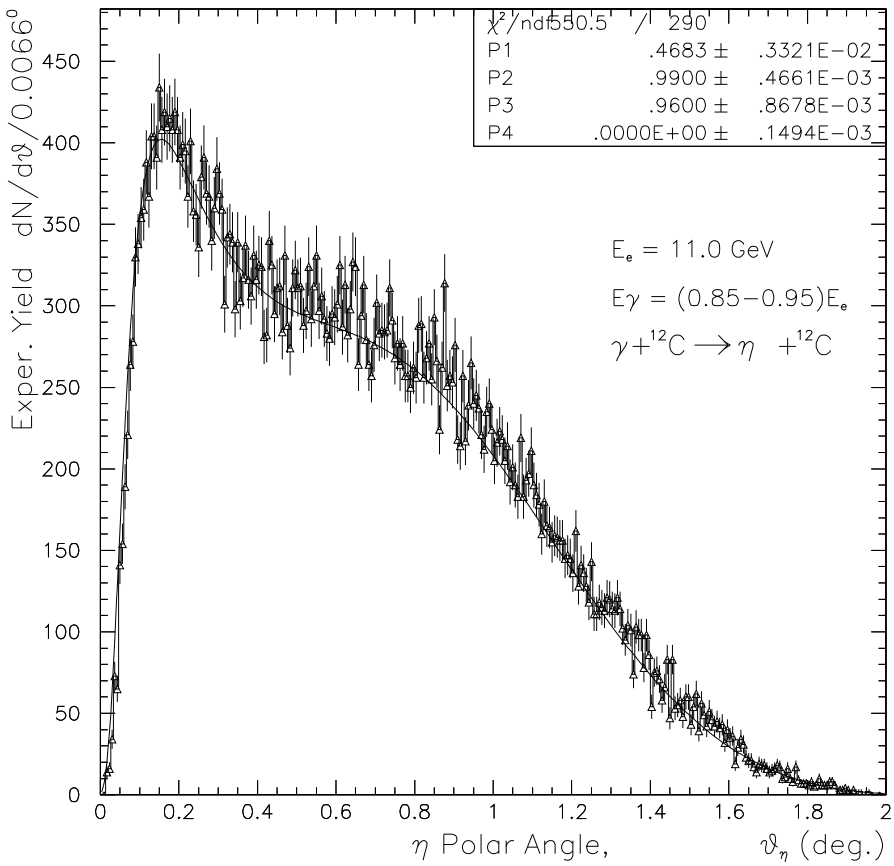

Figure 21: Monte Carlo simulation of experimentally measured angular distribution of $\eta\gamma\gamma$ events on ^{12}C.

to charge conjugation symmetry, however, the elastic Coulomb form factor (γPP) vanishes. The $\gamma^*\gamma P$ transition vertex, on the other hand, is of great interest and has been studied theoretically from the point of view of models based on the VDM as well as those involving treatments of the quark substructure[**?**][**?**]. This transition is characterized by the form factor $F(q_1^2, q_2^2)$ which, if only one photon has significant mass, depends upon a form factor typically parameterized, for the pion case, by the pole form (9), and approximated at low q_μ^2 by:

$$F_{\gamma^*\gamma\pi^o} \approx 1 - a\frac{q_\mu^2}{m_\pi^2}. \tag{34}$$

where a is a measure of the $\gamma^*\gamma\pi^o$ interaction radius.

The low, as well as high, Q^2 behavior of this form factor has been the source of considerable theortical effort. Recently, Maris and Tandy have used the ladder Bethe-Saltpeter solution for the dressed photon-quark vertex to study the low momentum behavior using model parameters fixed by the light meson masses and decay constants. They show that the often-used Ball-Chiu ansatz for the vertex is deficient. The results of their calculation are shown below, where the dot-dash line uses the bare vertex, the dashed is th Ball-Chiu

ansatz, and the solid line is their calculation.

figure 1(b) Maris

Frank, *et al.*, have calculated $F_{\gamma^*\gamma\pi^o}$ from a generalized impulse approximation within a QCD-based model field theory which gives a good description of the charged pion form factor. Their approach uses dressed vertices and propagators consistent with dynamical chiral symmetry breaking, gauge invariance, quark confinement, and perturbative QCD.

Their results are shown below where they find a $\pi\gamma\gamma$ interaction radius of $0.47fm$.

figure 2 Frank

Ivanov and Lyubovitskij calculate the form factor within a Lagrangian quark model with a separable interaction known to provide a good description of the pion observables at low energies. With their gaussian pion-quark vertex, they obtain an $r_{\pi^o} = 0.65fm$. Their results

are indicated by the dashed line in the following figure.

Ivanov

4.1 Previous Measurements in the Space-like Region

The CELLO collaboration at PETRA has measured $F_{\gamma^*\gamma P}$ in the space-like region at large momentum transfers using the reaction $e^+e^- \rightarrow e^+e^-P$[**?**]. In this experiment two photons are radiated virtually by the colliding e^+e^- beams. One of the virtual photons is close to real and the other has a larger q_μ^2 and is tagged by the detection of an e^+ or e^-.

Measurements were taken at momentum transfers ranging from 0.62 to 2.17 $(GeV/c)^2$, and the value of a was deduced by extrapolation under the assumption of vector meson dominance. For the pion, the authors quote a value of $a = 0.0325 \pm 0.0026$ (statistical) with systematic errors estimated to be of the same order as the statistical error. The results of these measurements are shown in figure 1 with the corresponding fits to $F_{\gamma^*\gamma P}$. Data covering

the q_μ^2 region from 2 to 20 GeV^2 have also been reported by the CLEO collaboration[**?**].

CELLO data

A conditionally approved experiment in Hall A (E97-009) will measure this form factor in the very low q_μ^2 regime ranging from 0.005 to about 0.035 $(GeV/c)^2$ to extract a. This leaves the intermediate momentum transfer region largely unexplored experimentally. The advent of 12 GeV electrons at TJNAF, however, will make such studies possible.

4.2 Previous Experiments in the Time-like Region

A number of experiments aimed at measuring a have been performed in the time-like momentum transfer region utilizing the π^o Dalitz decay $\pi^o \to e^+e^-\gamma$ reaction[3-12] The amplitude for this process involves the $F_{\gamma^*\gamma\pi^o}$ form factor which, in the usual linear expansion

$$F(x) \approx 1 + a\frac{m_{e^+e^-}^2}{m_{\pi^o}^2}. \tag{35}$$

a	reference
$+0.025 \pm 0.014 \pm 0.026$	Meijer Drees, 1992 [?]
$+0.026 \pm 0.024 \pm 0.048$	Farzanpay, 1992 [?]
$-0.11 \pm 0.03 \pm 0.08$	Fonvielle, 1989 [?]
$-0.01 + 0.08 - 0.06$	Gumplinger, 1987 [?]
$0.12 + 0.05 - 0.04$	Tupper, 1983 [?] (reanalysis of [?])
$+0.10 \pm 0.03$	Fischer, 1978 [?]
$+0.02 \pm 0.1$	Burger, 1972 [?]
$+0.01 \pm 0.11$	Devons, 1969 [?]
-0.24 ± 0.16	Samios, 1961 [?]
-0.15 ± 0.10	Kobrak, 1961 [?]

A summary of these measurements is shown in the table above, where it can be seen that the published values for the slope range from -0.24 to $+0.12$. Such experiments suffer from small kinematically accessible ranges and significant backgrounds, and they require large final-state radiative corrections. As such, these experiments have not been able to determine even the sign of the form factor slope.

4.3 The Proposed Experiment

In 1989, Hadjimichael and Fallieros[?] suggested that the virtual Primakoff effect, figure x, could access additional fundamental information about the pion as the cross section is proportional to $|F_{\gamma^*\gamma\pi^o}(q_\mu^2)|^2$. The full expression for the virtual Primakoff scattering cross section is[?][?]:

$$\frac{d^3\sigma}{d\epsilon_2 d\Omega_2 d\Omega_\pi} = \frac{Z^2\eta^2}{\pi}\sigma_M \frac{Q^4}{K^4}\frac{\beta_\pi^{-1}}{\omega_\pi}|F_N(K^2)|^2|F_{\gamma^*\gamma\pi^o}(q_\mu^2)|^2 sin^2(\frac{\theta_e}{2})sin^2(\theta_\pi)[4\epsilon_1\epsilon_2 sin^2\phi_\pi + |\vec{q}|^2/cos^2(\frac{\theta_e}{2})] \tag{36}$$

where σ_M is the Mott cross section, $\eta^2 = (4/\pi m^3)/\tau$, τ is the π^o lifetime, K is the (nearly real) photon four momentum from the Coulomb field, the pion four momentum is $Q = (\vec{q}, \omega_\pi)$, $\beta_\pi = \vec{q}/\omega_\pi$, and $F_N(K^2)$ is the nuclear form factor. This expression for the cross section in similar to equation x, except for the form factor $|F_{\gamma^*\gamma\pi^o}(q_\mu^2)|^2$ which is of interest here.

Hadjimichael and Fallieros examined the sensitivity of the cross section to a for energy transfers up to 1.6 GeV. They saw only moderate sensitivity and noted that the cross section is optimized for $\theta_e \to 0$ and $\theta_\pi \to 0$ whereas pion energies above 2 GeV are favored for probing the $\gamma^*\gamma\pi^o$ vertex. We have extended these calculations to kinematical regimes available with the proposed 11 GeV electron beam at TJNAF and note that good sensitivity to the $\gamma^*\gamma P$ form factor is present.

Figure22 shows the cross sections for the virtual Primakoff pion photoproduction process on helium-4 as a function of $E_{e'}$, an electron scattering angle of 2 degrees and a pion angle of

0.1 degrees with respect to $\vec{q}$. The incident energy is 11 GeV. The two curves are for the VDM prediction ($a = 0.03$) and that using the slope parameter determined by the $\pi^o \rightarrow e^+e^-\gamma$ experiment ($a = 0.1$) of reference [**?**]. From the plot one can see that the cross sections are large, and are quite sensitive to the pion transition form factor. If we define a figure of merit to be the difference in the predicted cross section for the two form factors times the square root of the average cross section, figure **??**, we see that the optimal kinematics are at θ_e=2 degrees and $\omega \approx 6$ GeV.

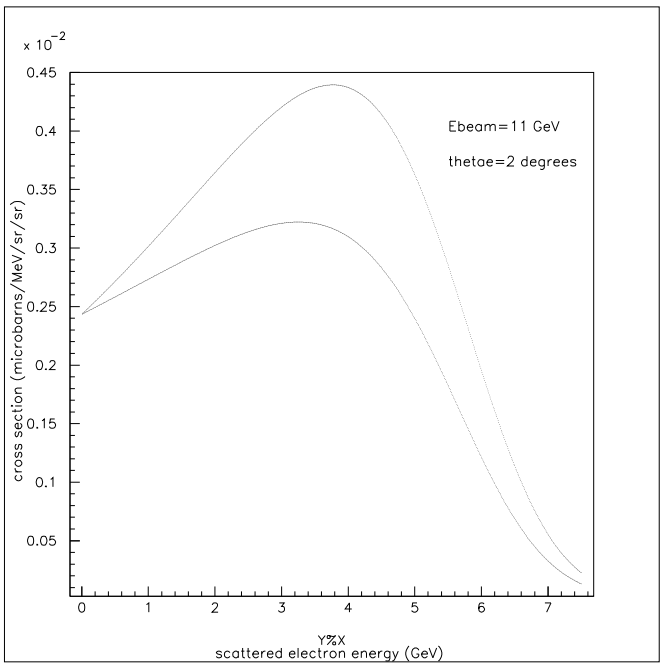

Figure 22: Cross section *verses* scattered electron energy for π^o production on helium-4. The incident electron energy is 11 GeV.

4.3.1 Experimental Setup for Transition Form Factor Measurements

We have investigated the Q^2 acceptance available for an experimental setup in which both the scattered electron and the two photons from the meson decay are detected in the previously described hybrid calorimeter (see figure reftffsetup). The calorimeter is $1.5m \times 1.5m$, is $7m$ downstream of the target, and has a $12cm \times 12cm$ central hole to allow the beam to pass through. For such a setup, the phase space for Q^2 acceptance is shown in figure 25 where a 1 GeV energy cut has been imposed on the scattered electron and the incident beam energy is 11 GeV. If one restricts the electron scattering angle and energy transfer to regions in which the figure of merit is largest (θ_e between 0.5 and 6 degrees, ν between 2 and 10 GeV), one obtains the Q^2 phase space shown in figures 26 and 27, where figure 27 shows the very

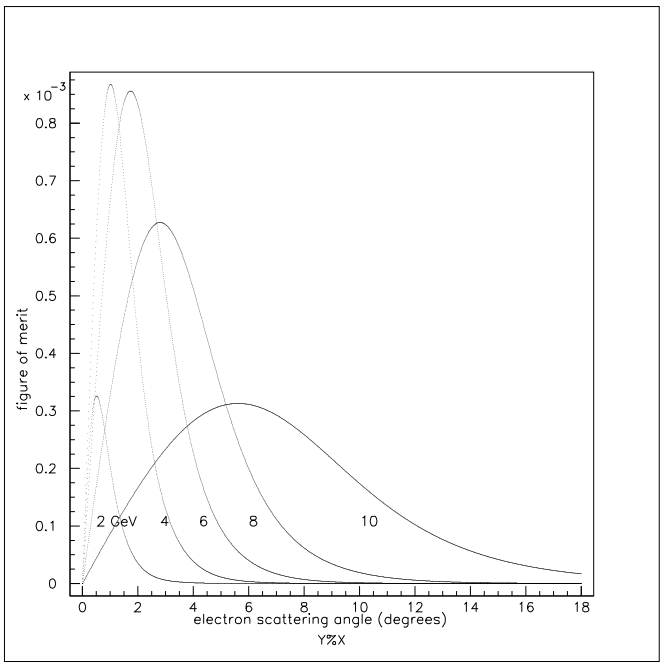

Figure 23: Figure of merit (see text) *verses* electron scattering angle for π^o production on helium-4. The incident electron energy is 11 GeV, and the various energy transfers are indicated.

low Q^2 acceptance. It can be seen that this setup complements the CELLO measurements in covering the extremely low Q^2 region which is unavailable to the collider experiments.

Figures 28 and 29 show the resolutions in Q^2 at $Q^2 = 0.01 GeV^2$ and $Q^2 = 0.5 GeV^2$, respectively, resulting from finite position and energy resolutions in the detection of the scattered electrons in the hybrid calorimeter. It can be seen that the Q^2 resolution is more than adequate to extract the Q^2 dependence of $F_{\gamma\gamma^* P}$.

4.3.2 Rates for $F_{\gamma\gamma^*\pi^o}$ and $F_{\gamma\gamma^*\eta^o}$

Figure 30 shows the cross section as a function of θ_π for Primakoff, coherent nuclear, and interference photoproduction processes. It can be seen that clean separation is possible. The analogous curves for the η figure of merit and cross section are shown in figures 31 and 32.

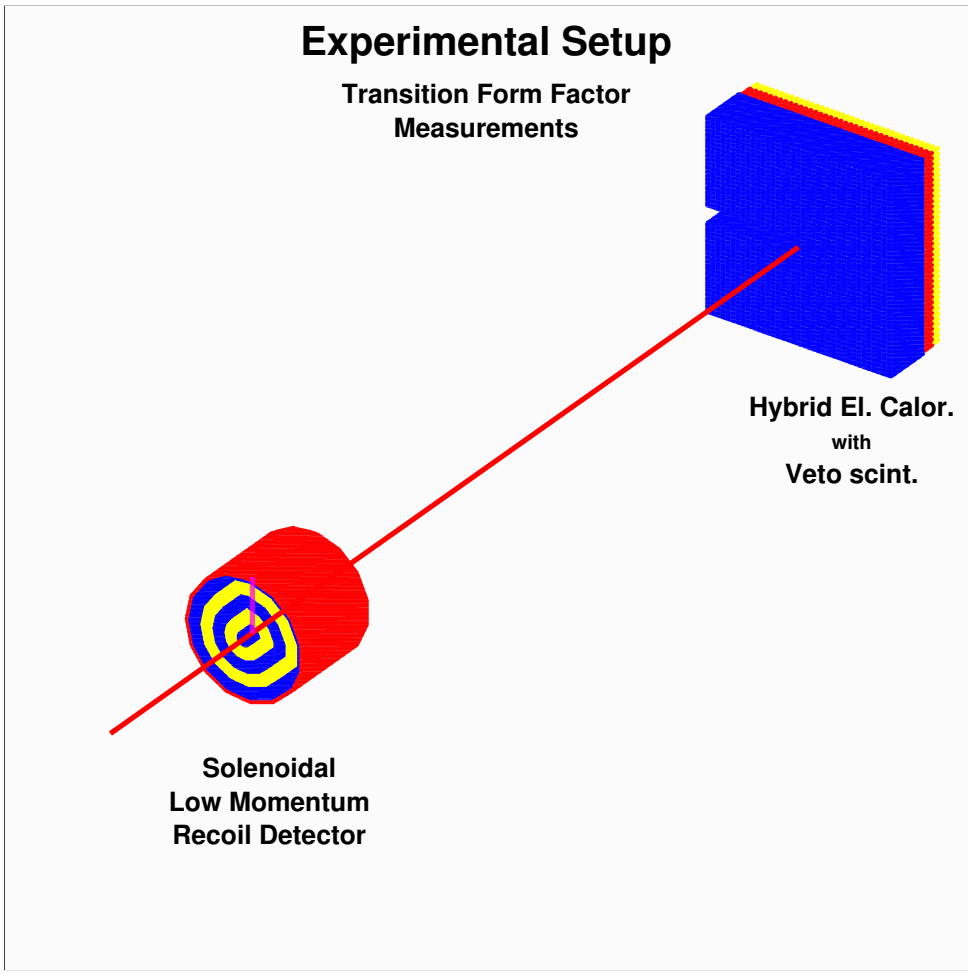
Experimental Setup
Transition Form Factor
Measurements
Hybrid El. Calor.
with
Veto scint.
Solenoidal
Low Momentum
Recoil Detector

Figure 24:

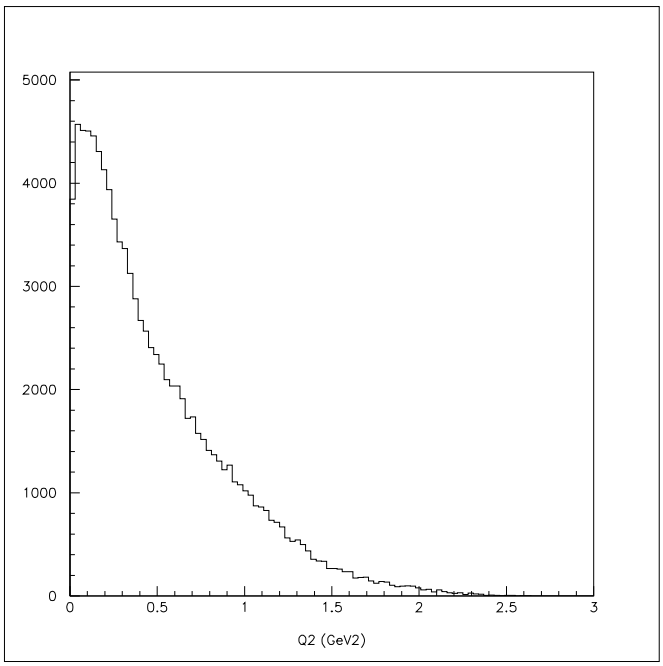

Figure 25: Phase space for Q^2 acceptance of a $1.5m \times 1.5m$ detector with a $12cm \times 12cm$ central hole. Detector is 7 m from target. A 1 GeV energy cut is imposed.

With this experimental setup, we expect a yield of 3900 π^o's and 600 η's per day. This assumes a 10^{-5} radiation length ^4He target, and a $5\mu Amp$ 11 GeV electron beam. The two photon acceptance of the hybrid calorimeter was taken to be 50%, and the branching ration for two photon decay of the η was taken to be 39%.

5 Summary

We have described a comprehensive program to measure the electromagnetic properties of pseudoscalar mesons which would be possible with advent of 11 GeV CW electron beams at Jefferson Lab. Precise measurements of the two photon widths and transition form factors would provide stringent tests of both QCD and QCD based models. We believe the proposed instrumentation to be constructed for this program will be of general use to both this program, and future experiments.

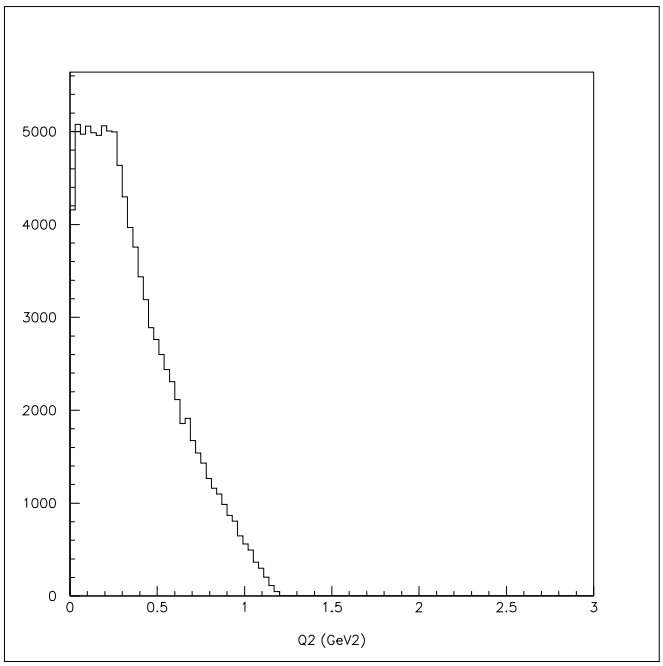

Figure 26: Phase space for Q^2 acceptance of a $1.5m \times 1.5m$ detector with a $12cm \times 12cm$ central hole. Detector is 7 m from target. Scattering angle is between 0.5 and 6 degrees. Energy transfer is between 2 and 10 GeV.

References

[1] J.S. Bell et al., Il Nuovo Cimento, vol. 51, no. 1., (1969), 4

[2] S. Adler, Phys. Rev., vol. 177, no. 5, (1969), 2426.

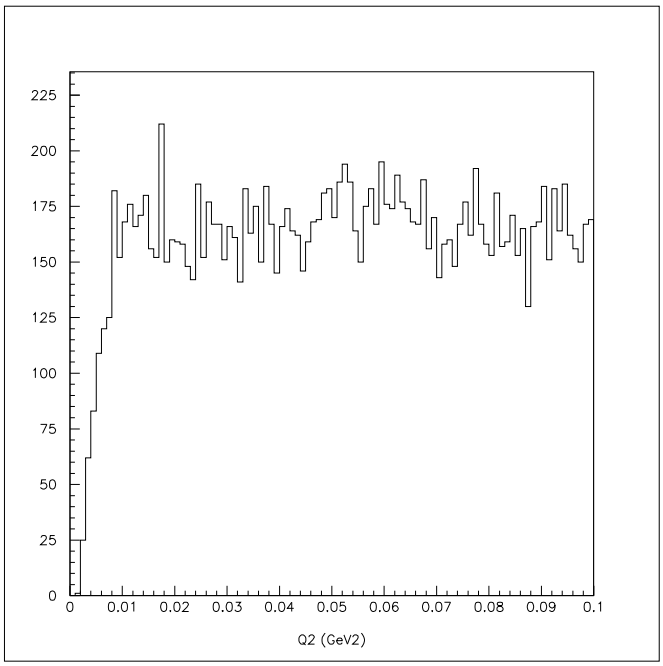

Figure 27: Phase space for Q^2 acceptance of a $1.5m \times 1.5m$ detector with a $12cm \times 12cm$ central hole. Detector is 7 m from target.Scattering angle is between 0.5 and 6 degrees. Energy transfer is between 2 and 10 GeV.

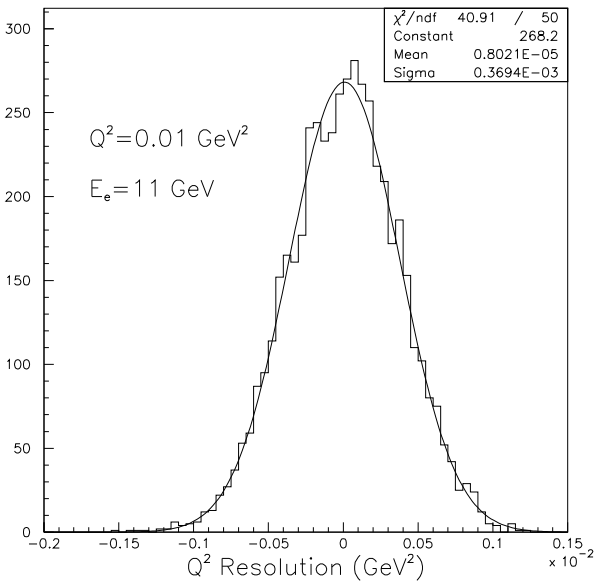

Figure 28: The diference in actual *verses* reconstructed Q^2 resolution for $Q^2 = 0.01 GeV^2$.

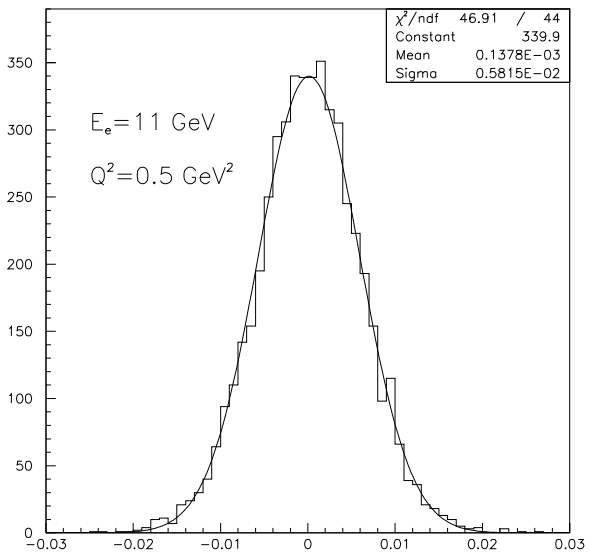

Figure 29: The diference in actual *verses* reconstructed Q^2 resolution for $Q^2 = 0.5GeV^2$.

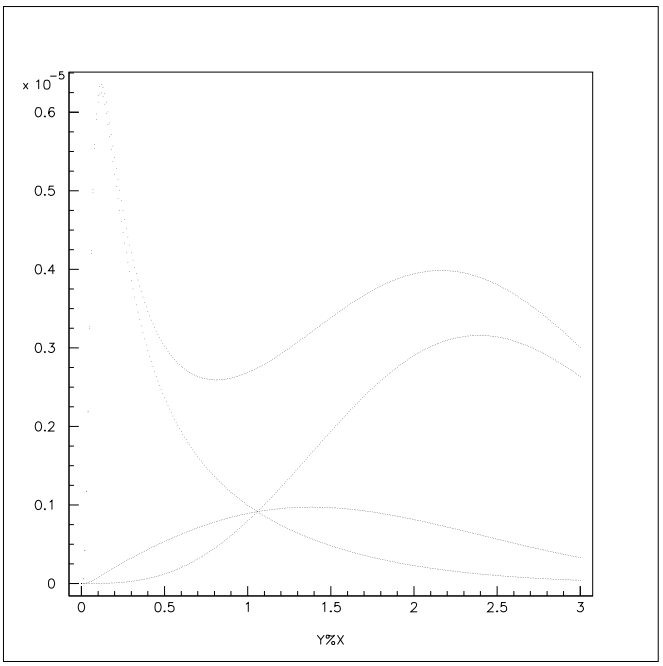

Figure 30: Cross section *versus* θ_π weighted by $sin(\theta_\pi)$ showing Primakoff, nuclear coherent, and their interference.

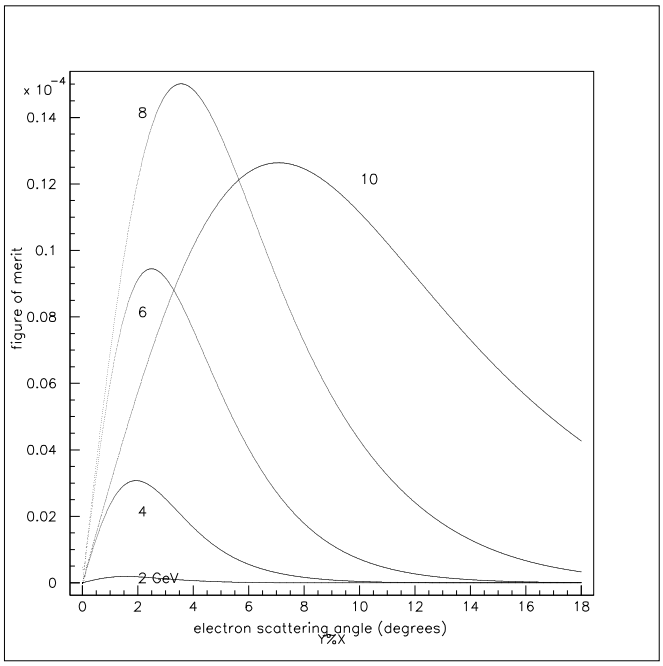

Figure 31: Figure of merit (see text) *verses* electron scattering angle for η production on helium-4. The incident electron energy is 11 GeV, and the various energy transfers are indicated.

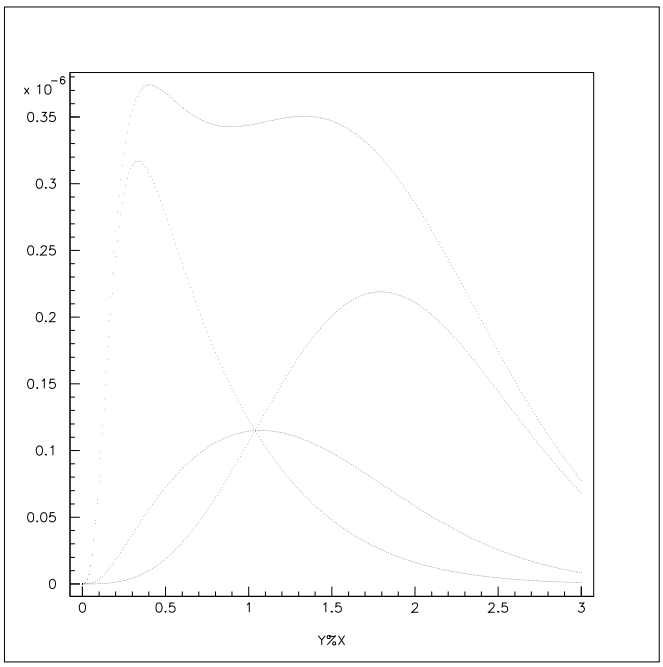

Figure 32: Cross section *versus* θ_η weighted by $sin(\theta_\pi)$ showing Primakoff, nuclear coherent, and their interference.